Extraction of the Total Photabsorption Cross Section for ^{24}Mg

Jacob Andries Cornelius Bekker

A dissertation submitted to the Faculty of Science,
University of Witwatersrand in fulfillment
of the requirements for the degree of Master in Science

Department of Physics
University of Witwatersrand
South Africa
December 2021
Supervisors:
Dr L. Pellegri
Prof M. Wiedeking
Dr P. Adsley

This work is based on the research supported in part by the National Research Foundation (NRF) of South Africa grant number 118846.

Declaration

I declare that this thesis is my own, unaided work. It is being submitted for the Degree of Master of Science at the University of the Witwatersrand, Johannesburg. It has not been submitted before for any degree or examination at any other University.

Date:2022/03/11

Jacob Andries Cornelius Bekker 

Acknowledgements

In the great tumult of the past two years, my principal supervisor Luna Pellegri has remained compassionate and patient with me during the course of this project. While the meetings and communications were virtual and remote, her guidance was inspired and for that I'm eternally grateful.

To my co-supervisor, Philip Adsley, for being the encyclopedic reference that both Sifundo and I could count on when tackling problems that seemed to have stranger roots than we could imagine. His persevering humour during even the worst of all English batting collapses has given me reason to believe there is even hope for me to one day become a scientist even after multiple severe neural misfires.

To my other co-supervisor, Mathis Wiedeking, for giving me the opportunity to work with all the wonderful people at iThemba LABS and become part of that community.

To my family: Emmie for the company and go getting attitude that I so desperately need at times. My father for the head scratching moments of confusing but still proof reading it anyway. My mother for being the steersman of our abode when the entire world felt like it needed a mothers' touch. My brother, Petros, for being my closest ally and dearest friend. None of this could have been remotely possible without any of you.

To the men of culture, Hanru and Brand, your friendship has turned what would have been a calamity of a year into a time that I will treasure.

To Dhané, for being the reason I wake and want to be an even better version of myself every morning. Your critical eye for graphics will likely cause me lose some of the blissful sleep I get knowing that you are by my side.

To Grietjie Bekker, the warmest black hole to ever grace a human lap.

Abstract

Accurate nuclear data is a key factor in determining the suitability and reliability of many theoretical nuclear models and large-scale calculations. One of the main components of these calculations is how nuclei respond to an electromagnetic field. The excitation of the isovector giant dipole resonance (IVGDR) is of particular importance in both nuclear structure studies as well as being the main mode of interaction of ultra-high-energy cosmic rays with the extragalactic medium en route to Earth. This study investigates the photoabsorption cross section in the region of the IVGDR in ^{24}Mg through the use of proton inelastic scattering and the equivalent virtual photon method. The K600 spectrometer at the iThemba LABS facility was used to obtain high resolution, low background ^{24}Mg(p,p')^{24}Mg* inelastic scattering data. The virtual photon absorption method proved effective and the photoabsorption cross section is in agreement with the broad structure of previous data using real photons and improved on the fine structure thereof.

Contents

1 Introduction **10**

2 Theoretical Considerations **14**
2.1 Giant Resonances 14
2.2 Photo-excitation 24
2.2.1 Coulomb Excitation 24
2.2.2 Classical Excitation 24
2.2.3 Semi-Classical Excitation 25
2.2.4 Virtual Photons Excitation 27

3 Experimental Setup **31**
3.1 iThemba LABS facility 31
3.2 The K600 spectrometer 33
3.2.1 Focal Plane Detection Suite 33
3.2.2 Data Acquisition System 38
3.2.3 Target Carousel 39
3.2.4 Zero Degree Mode 39
3.3 Experimental Procedure 41
3.3.1 Halo Optimization 41
3.3.2 Dispersion Matching 42
3.3.3 Faint Beam Method 45

4 Data Analysis **47**
4.1 Data Extraction 47
4.1.1 PID (Particle Identification) 47
4.1.2 Cable Length Offsets 48
4.1.3 Look Up Tables (LUT) 49
4.1.4 Angle Calibrations 54
4.1.5 Position Offsets 57
4.1.6 Lineshape Corrections 57
4.2 Preparation of data 59
4.2.1 Background subtraction 59
4.2.2 Energy Calibration 62
4.2.3 Cross section calculation 64

5 Results and Discussion **68**
5.1 Virtual photon production 69
5.2 Photoabsorption Spectrum 73
5.2.1 Comparison to previous data sets 74
5.2.2 Angular Sensitivity Analysis 77

6 Conclusion and Outlook **82**

List of Figures

1.1 All particle spectrum for UHECR 11
1.2 An illustration of one of the possible photodisintegration decay chains 12

2.1 A comparison between experimental data (dots) and RPA calculations (lines) for ^{90}Zr,^{120}Sn and ^{208}Pb. 16
2.2 Schematic representation of the different macroscopic resonance modes showing the differences between GRs. 16
2.3 Figure showing different macroscopic model representations of the IVGDR 18
2.4 Graph showing the inverse dependence of centroid energy on atomic mass for the GDR [32]. 19
2.5 An illustration of the wavelength associated with a standing wave in a spherical nucleus. 20
2.6 Schematic representations of the width of GRs. 22
2.7 Graph showing the systematic Lorentzian calculations for positions of the ISGMR [37], IVGDR [38] and the ISGQR [39]. . . . 23
2.8 A schematic description of Rutherford scattering where the projectile follows a hyperbolic path [48] 25
2.9 Comparison between the Eikonal model and the semiclassical model virtual photons per unit solid angle for 296 MeV protons incident on a ^{154}Sm target at different scattering angles (degrees).[53] 30

3.1 A schematic representation of the iThemba LABS SSC facility. The main beamlines are shown along with the various beam splits towards different detectors/experiments [54]. 32
3.2 The schematic zero-degree configuration of the K600 spectrometer showing beam dispersion. 34
3.3 A photo and schmatic of the focal plane detection package . . . 36
3.4 A calculation using Garfield software of the VDC field lines and a hypothetical proton track moving through it. 37
3.5 A drift time spectrum of the accepted events in a run. 38
3.6 A typical layout of the trigger electronics used in K600 experiments.[54] 40

3.7 The target ladder used in the PR210 experiment [55]. 41
3.8 The 45° beam viewer known as the Hatanaka mesh [57]. 42
3.9 A photograph showing the target frame used in the PR210 experiment. 43
3.10 A representation of charged particle paths under different dispersion matching conditions. 45
3.11 Meshes that retain the ion-optic characteristics of the beam but reduce the beam intensity by a factor of 10000. 46

4.1 2-D ToF versus energy deposition spectra in ^{24}Mg. 48
4.2 Drift time spectra before and after cable length corrections. . . . 50
4.3 A schematic representation of how a charged particle is characterised in the drift cells. The positive and negative drift distances indicate which direction the ionised molecules drift in the drift cell and W_{min} is the center of the drift cell through which the particle crosses. 51
4.4 2-D Resolution plots before implementation of the LUT offsets . 52
4.5 2-D Resolution plots after implementation of the LUT offsets . . 53
4.6 Figure showing the effect of the LUT offsets. 54
4.7 Photo of the pepperpot collimator used during experiments. The holes each span 0.41^0 and the centroids are 0.81^0 degrees apart. 55
4.8 Figure showing the focal plane angle obtained from the pepperpot run and an example of the Gaussian fit used to obtain the centroid of each hole. 55
4.9 The graphs used for angular calibration. 56
4.10 The combined position spectrum of ^{24}Mg showing the difference in the position spectrum before (red) and after (blue) offsets were introduced. 57
4.11 Figure showing a the 10.711 MeV state in ^{24}Mg before lineshape correction (top) and after lineshape correction (bottom). 58
4.12 The fifth order polynomial (blue line) generated by fitting the unaligned 10.711 MeV state of ^{24}Mg at 660 mm. 59
4.13 The net effect of the lineshape corrections are seen in the increase of the peak resolutions from the top panel to the bottom panel. 60
4.14 Enhanced image showing the regions of interest for the background subtraction. 61
4.15 Comparison of different background regions for the ^{24}Mg spectrum. 62
4.16 The background unsubtracted (blue) and background subtracted spectra (red). 63
4.17 Plot showing the quadratic energy fit to focal plane position of the 9.305, 10.711 and 12.954 MeV states. 64
4.18 The count spectrum after being converted from focal plane position to excitation energy. 65
4.19 Spectrum showing the Double Differential Cross Section obtained from the excitation energy spectrum. 67

5.1 A DWBA calculation on ^{142}Nd showing the contribution of the coulomb and nuclear interactions combined and separately. . . . 70
5.2 The double differential cross section for (p,p')^{124}Sn at 200 MeV. 71
5.3 The virtual photon production spectra for ^{24}Mg. 72
5.4 The E1 photoabsorption cross section versus excitation energy spectrum. The IVGDR becomes visible in this spectrum as an increase in strength between 14 and 23 MeV. 73
5.5 The E1 photoabsorption cross section the after it has been rebinned and normalised. 75
5.6 The section of the spectrum highlighting the significant difference between the previous (γ, abs) [67] experiment and the (p,p') spectrum near the neutron threshold. 76
5.7 The contributions from the ISGQR and phenomenological background calculated for a similar experiment at iThemba LABS. . . 77
5.8 The counts spectrum for each angular region following the background reduction 78
5.9 Results of the angular sensitivity analysis. 80
5.10 A schematic of the aperture showing the solid angle of the detector. The red region corresponds events that can be mapped to a scattering angle between 0° and 1° due to poor vertical resolution and the gray to 1° and 2°. 81

List of Tables

3.1 The technical specifications of the focal plane detectors used in this experiment [54]. 35
3.2 The dispersion matching settings of the K600 spectrometer for high dispersion, 200 MeV protons. 45

4.1 Table of the LUT offsets used for this data. 51
4.2 θ_{fp} to θ_{scat} conversion coefficients 55
4.3 List of lineshape correction coefficients. 59
4.4 Focal plane to energy conversion coefficients 63
4.5 Peak energies and uncertainties compared to their known values [62]. 64
4.6 Sources of error in the cross section calculation. 67

Chapter 1

Introduction

In the current era of post-Higgs physics, there still exist many unanswered questions about high-energy particles, and more specifically about, ultra high energy cosmic rays (UHECR). The first observation of UHECRs was in 1963 by Dr John Linsey at Volcano Ranch in New Mexico [1] and since then the search for their origins and propagation mechanics has been prolific. An UHECR is an observed particle with energy in excess of 1×10^{14} eV per nucleon with the most energetic specimens believed to be iron nuclei [2]. While it has been verified that these energetic particles exist and are relatively rare (the Pierre Auger Observatory reports an average of 27 observations every four weeks [3]), there is limited knowledge of what generates them and how they propagate through space. The general consensus is that these nuclei or protons are accelerated extra-galactically with a speculated origination hotspot in the Ursa Major constellation [4]. UHECR are important because they probe a range of energy that is significantly closer to the Plank energy scale than is currently achievable on Earth and they can potentially serve as informants about theories beyond the Standard Model. A comprehensive study of these nuclei requires a theoretical approach to modelling the interactions that UHECRs experience. This will help constrain the limits to their lifespan and travel time, while also providing information about possible origination sites.

The attenuation mechanics of UHECRs traveling from the source to Earth are related to their interactions with the cosmic microwave background (CMB). As shown in Fig.1.1, these UHECRs occupy a spectrum that ranges well into 10^{20} eV's. The Lorentz boost factor, Γ, an increase in perceived energy due to the differences in linear momentum between two objects, experienced by the CMB from the UHECR reference frame causes high energy photons to be encountered by the nucleus. Lorentz boost factors of between $\Gamma = 10^{8.5}$ and $\Gamma = 10^{9.5}$ [6] cause the CMB to be blue-shifted towards energy ranges of a few MeV. This means that CMB photons can excite the giant dipole resonance (GDR) in these nuclei. The photons are absorbed, inducing photodisintegration mechanisms which cause an energy dissipation and disintegration of the original UHECRs

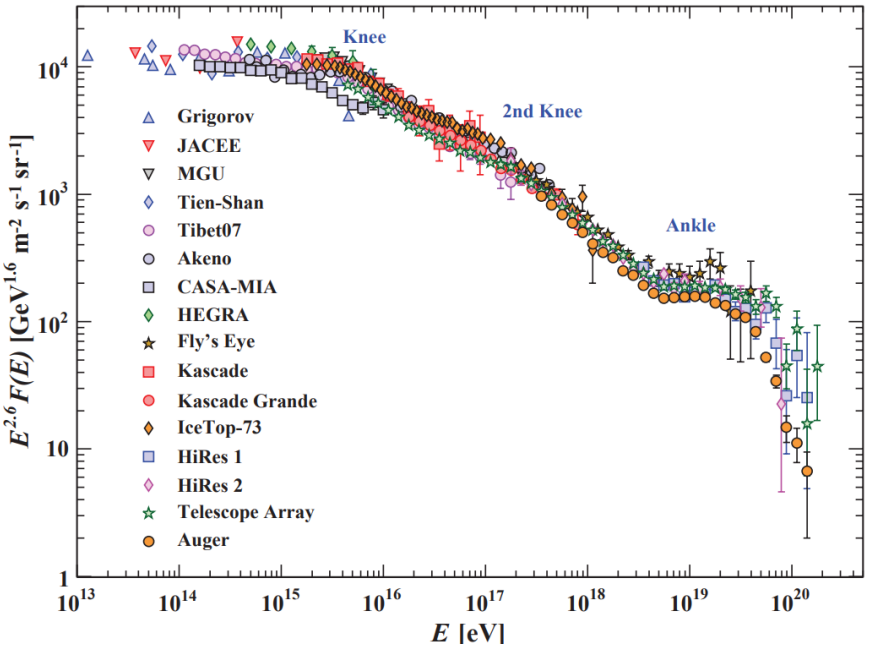

Figure 1.1: All particle spectrum for UHECR showing both the knee at 1×10^{16} eV and ankle of the spectrum at 1×10^{19} eV [5].

nuclei. If the photodisintegration reaction rates, cross-sections, energy and mass losses could be accurately determined, then the uncertainties in propagation distance and mass evolution would be limited to astrophysical quantities such as the galactic magnetic field. The maximum distance protons can travel has been named the GZK (Greisen, Zatsepin and Kuzmin) cutoff [7] and was based on assumption that the main interaction method for UHECR would be deflections by a magnetic field and interactions with the CMB. The GZK cutoff is a limit that only applies to protons while the limit for heavier nuclei is considerably harder to estimate. The byproducts of the proton interactions are secondary neutrinos and photons which can be detected by our observatories. With regards to nuclei, the byproducts become more complex given that they can be affected by other reactions that can also change their composition such as the (γ, α), (γ, n) or (γ, p) reactions.

The need for accurate nuclear data is evident given that a large portion of energy dispersion is directly related to the photodisintegration cross-section and the decay paths for each of the de-excitation modes [8]. The way in which these nuclei propagate relies on a series of photodisintegration paths, one of which is shown in Fig. 1.2. Iron nuclei, the heaviest observed thus far, can undergo a vast number of photodisintegration chains, some into unstable nuclei, before it

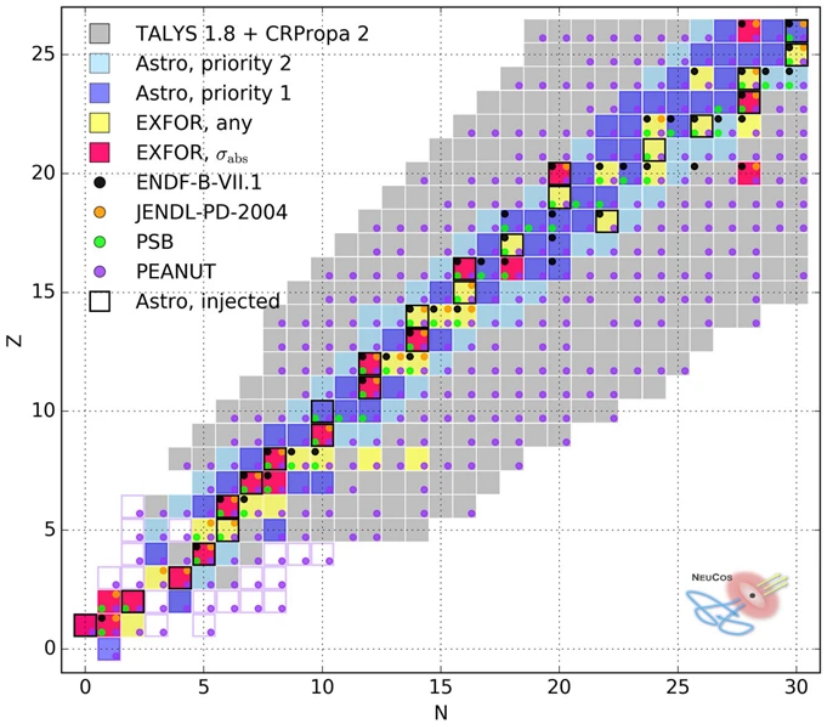

Figure 1.2: A nuclear chart that shows the nuclei of interest for UHECRs and indicates the information available for each of them. The important nuclei are shown in light and dark blue according to their relative astrophysical importance [11].

reaches the earth. Starting with an ^{56}Fe nucleus, it can react with the CMB and disintegrate via α, neutron, proton, deuteron or triton emission. In order to calculate the amount of energy lost accurate data for each of the branching rates is required. The same properties are required for daughter nuclei and this continues all the way down the atomic mass chart to A=2. In all of the current simulations for the propagation of UHECR, data for all the elements of interest with mass number less than 56 is necessary [9]. The total photoabsorption cross-section as a function of energy for only 10 nuclei in this range is known and the total integrated photoabsorption cross-section for 16 is known [10]. The lack of data combined with the problem that many of the calculated branching rates for light nuclei are highly unreliable, translates into predictions that cannot properly be constrained and are thus unreliable.
This shortage in nuclear data has given rise to the PANDORA (Photo-Absorption of Nuclei and Decay Observations for Reaction in Astrophysics) project with the goal being to systematically measure charged branching rates and photoabsorp-

tion cross sections for most of the keystone nuclei involved in astrophysics. The project is a multinational collaboration of astrophysicists and nuclear physicists with the majority of the experiments scheduled to occur at RCNP-Japan, iThemba LABS, South Africa and ELI-NP, Romania. This thesis serves as a preliminary assessment of the techniques used by the PANDORA project to investigate these nuclei.

The goal of this dissertation is to extract the photoabsorption cross section for ^{24}Mg in the energy range of the isovector giant dipole resonance using the virtual photon production method, the method primarily proposed for PANDORA measurements. Afterwards, a fit of the parameters of the theoretical Lorentzian to the cross section spectrum is obtained to verify if the systematics currently in use are accurate and whether this method also functions for highly deformed, light nuclei. This is precursor to the experiments planned for Project PANDORA and will mainly be used to test the techniques involved. The results of this investigation can be implemented in the astrophysical reaction code TALYS [12] for use in UHECR propagation codes such as CRPropa [13] and SIMprop [14] to gauge the net effect of new data on the current calculations.

Chapter 2

Theoretical Considerations

2.1 Giant Resonances

General Features

There are two main types of excitation in nuclei, single-particle and collective. Giant Resonances (GR) are nuclear excitation modes of the nucleus wherein a large percentage of the nucleons participate in a collective motion. This was first observed in 1937 by Bothe and Gentner when they noticed an enhanced absorption of intermediate energy photons by ^{63}Cu [15] and was later quantified by Goldhaber and Teller as a hydrodynamical effect based on out of phase neutron and proton fluid vibrations [16]. This is in contrast to nuclear resonances where only a few nucleons are involved in the interaction. As the name suggest, GRs are typically higher in energy and much wider than their single particle counterparts with energies of tens of MeVs and widths of a few MeVs. They appear in every nucleus except the lowest mass number few, where the concept of collectivity can be brought into question.

The excitation of GRs has proven to be a powerful tool for investigating nuclear structure. Quantities such as the shape and strength of the GRs can be used for theoretical model validation and can provide insight into some nucleus specific features like the effect of the nuclear surface in collective excitations [17]. One of the features that require investigation is the fragmentation of the giant resonances for non-spherical ground-shape nuclei such as ^{24}Mg. This fragmentation occurs due to the introduction of two axes along which the nucleons can oscillate.

Although the visualisation of GRs are generally macroscopic, the microscopic structure does play a role in determining the properties of the resonances [18]. An understanding of both descriptions is required to characterize GRs.

Microscopic Description

The microscopic description of a GR is not a computationally trivial problem due to the fact that there are many nucleons involved in a collective excitation and each nucleon exerts a potential on all the other nucleons leading to a many-body problem. The only theories that can be considered seriously are approaches which adhere to experimentally proven facts like the near exhaustion of the energy weighted sum rule by the GRs. Sum rules contain the relation between the integral of the strength distribution of all states and ground state properties and they can be determined model independently. A known property of GRs that fit this category is that they exhaust a large fraction of the sum rule [19].

The Random Phase Approximation (RPA) is the simplest many-body theory that shows good experimental agreement with the sum rule condition. According to RPA, GRs are produced by superpositions of single particle-hole (1p-1h) operators, $\hat{O}$, acting on the ground state configuration which induces coherent excitations [20]. Mathematically put:

$$\left|\Psi_{GR}^{\lambda,\sigma,\tau}\right\rangle = \hat{O}^{\lambda,\sigma,\tau}\left|\Psi_{GS}\right\rangle, \tag{2.1}$$

where λ, σ and τ represent the multipolarity, spin and isospin of the resonance and its associated operator. The intra-nucleon interaction is described in terms of a mean field and residual interaction. This is less demanding computationally as the individual intra-nucleon reactions can be approximated by a single nucleon interacting with the mean field. In this model, the mean field and residual interaction is generated using a functional that depends on the local spin, current and nucleon densities. The complete description of this method can be found in the literature [21][22][23].

RPA is effective at producing mean energies and total transition strengths and in some cases can be used to determine GR widths in deformed nuclei. Modern approaches use modified versions of RPA such as the Separable Random Phase Approximation that introduces second order Skyrme forces to describe deformed resonances [25]. An example of an RPA calculation using Skyrme forces is given in Fig.2.1. In general, the microscopic models used are case specific and do not cover the entire nuclear chart. As such, success with microscopic models have mainly been found in heavy nuclei where the statistical effects dominate [26] or in spherical light nuclei where numerical methods can converge [27].

Macroscopic Description

Macroscopic models are useful tools to describe the bulk behaviour of a nuclear system by modelling the behaviour of the whole nucleus rather than a single nucleon. The shell model is an example of such a model where nuclear structure is modelled using the Pauli-Exclusion principal and energy levels. The fundamental shell model interpretation of the nucleus assumes that the nucleus is

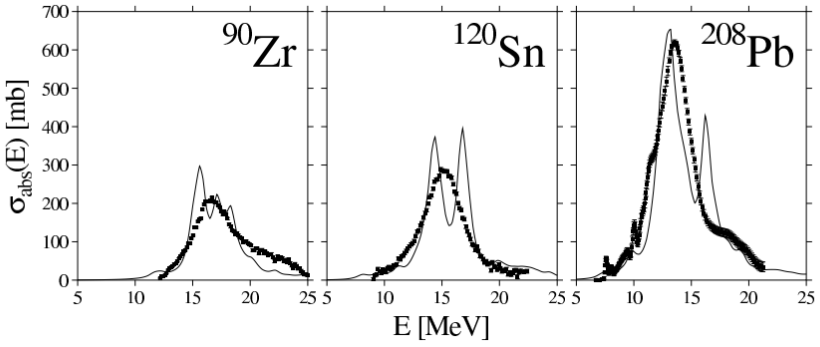

Figure 2.1: A comparison between experimental data and RPA calculations for ^{90}Zr,^{120}Sn and ^{208}Pb. The mean energies and widths of Isovector GDRs are in agreement with the experimental data from heavier isotopes [24].

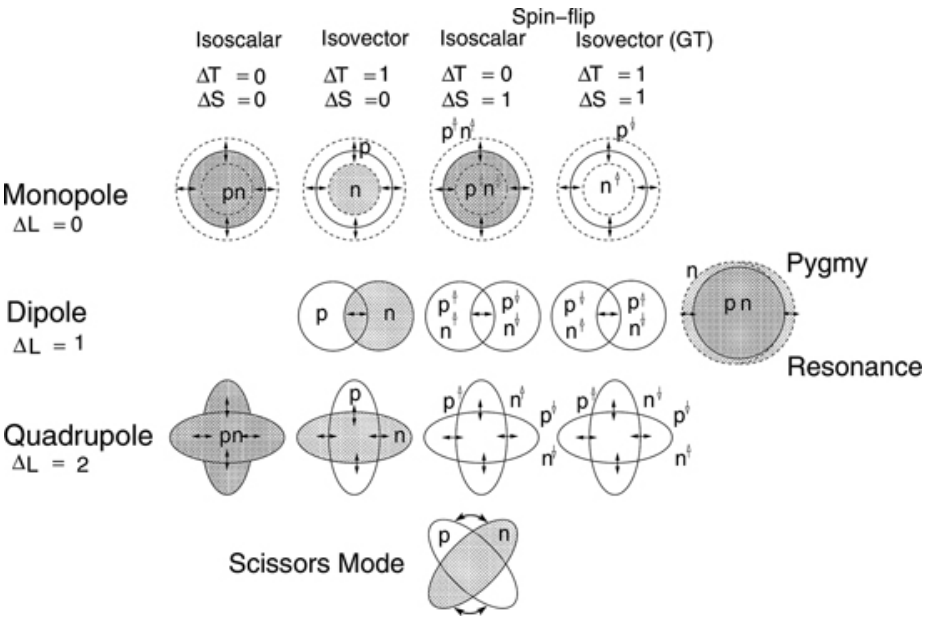

Figure 2.2: Schematic representation of the different macroscopic resonance modes showing the differences between isovector (IV) and isoscalar (IS) modes and the differences between multipolarities as well as the Gamow-Teller spin flip modes. The pygmy and scissors resonances are shown for completeness [28].

spherical, non-deformed and stationary [29]. In the case of the collective excitation of ^{24}Mg, this is clearly a naive approach and the more inclusive collective model is used to describe it. It is essentially a combination between the extreme

single particle theory and the liquid drop model [30]. The main types of collective excitation that arise from this description are vibrational modes for lighter nuclei ($A < 90$) and rotational modes for heavier nuclei ($A > 120$).
The vibrational mode of excitation of a giant resonance is generally viewed as a damped oscillation of a large portion of nucleons around the equilibrium shape of the nucleus. The shape and structure of these oscillations depend on the multipolarity, spin and isospin of the excited state. Different collective states can be described using their angular momentum, L, and are visualised as shown in Fig.2.2:

1) A monopole ($L = 0$) resonance has an oscillation with a radial expansion and contraction.
2) A dipole ($L = 1$) resonance is viewed as an oscillation along a central axis.
3) A quadrupole ($L = 2$) resonance has two planes of oscillation along the minor and major axes.

The isospin of the resonance differentiates between the nucleons that oppose one another's movements in the oscillation. If the isospin of the state is 0 ($\Delta T = 0$), protons mirror the movements of neutrons in the nucleus creating charge asymmetry in the nucleus, whereas isospin ($\Delta T = 1$) resonances occur when the protons and neutrons oscillate in a manner in which the charge density of the nucleus stays constant. The spin of the resonance differentiates between the spin up and spin down nucleons. There are resonances with higher multipolarities such as the giant octupole resonance but the resonances of interest when discussing virtual photoabsorption are mainly the IVGDR, ISGQR and the ISGMR.

The systematic calculations that lead to theoretical predictions of the energy of IVGDR are based on a combination of two macroscopic interpretations, namely the Goldbach-Teller (GT) [16] and the Steinwedel-Jensen (SJ) model [31].
In the former, a charged particle exerts an electric field on the protons of the nucleus and induces an opposite phase oscillation between the protons and neutrons. In this calculation the incompressiblity of both sets of nucleons is separately kept constant as shown in Fig. 2.3. This leads to a $A^{-1/6}$ energy dependence based on classical calculations using the frequency of the vibrations of the nucleons.
In the Steinwedel-Jensen model, the nucleons are released from the separate incompressiblity requirement and are instead subjected to the surface of the nucleus being incompressible. The oscillation is then treated using proton and neutron densities in such a way that a deficit in proton density is mirrored by an abundance in neutron density. This, in turn, leads to a resonance energy variation with $A^{-1/3}$.

The systematic energy calculations for IVGDRs that are currently used are based off of a combination of these two models and leads to an equation for resonance energy, E_R, of the following form [33]:

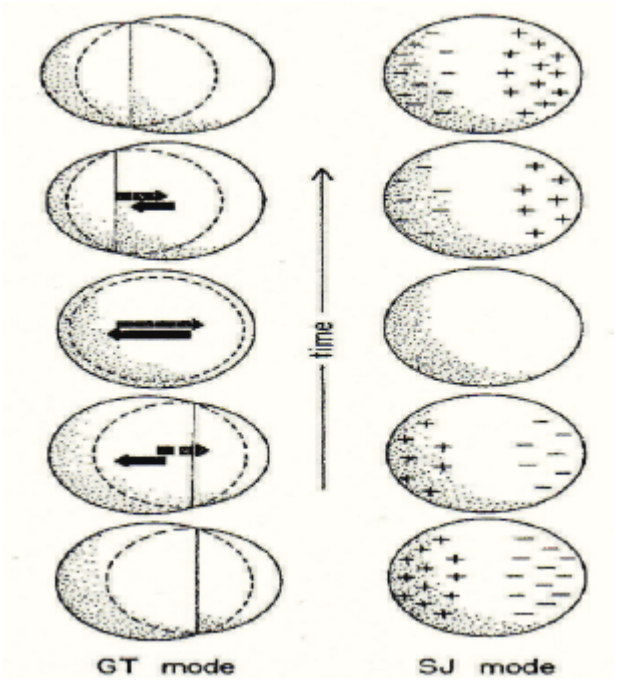

Figure 2.3: The left hand side shows the interpretation of the incompressiblility being preserved in the GT model and the right hand side shows the incompressible skin with the proton and neutron density fluxes.

$$E_R = 112 \times (A^{2/3} + 276 \times A^{1/3})^{-1/2}. \tag{2.2}$$

The predictions of IVGDR energy and measured values are shown in Fig. 2.4. In general, the GDR structure can be described using a superposition of Lorentzian functions that are paramaterised by the energy and the width of the resonance[33]:

$$\sum_{i=1} \sigma_i(E) = \sigma_{mi} \frac{\Gamma_i^2 E_i^2}{(E_i^2 - E_{mi}^2) + E_i^2 \Gamma_i^2}. \tag{2.3}$$

In this equation E_i^2 represents the excitation energy, σ_{mi} the peak resonance cross section, E_{mi} the peak resonance energy and Γ_i the resonance width. The index of the summation is determined by the deformation of the ground state nucleus. Spherical nuclei have one axis of vibration and hence the Lorentzian has only one term. For bi-axially deformed nuclei such as ^{24}Mg, the IVGDR is split into two parts, K_0 and K_1, and is described by the superposition of

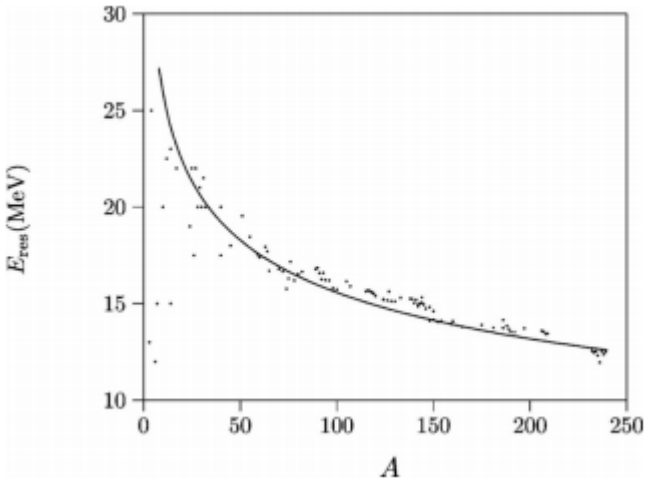

Figure 2.4: Graph showing the inverse dependence of centroid energy on atomic mass for the GDR [32].

two Lorentzians. The K_0 and K_1 splitting of the IVGDR is due to the nucleus having two axes along which it can vibrate. The vibration along the semi-major axis requires slightly more energy than vibration along the major axis and leads to the K_0 mode being located at lower energies than the K_1 mode. This can be understood according to the wavelength of the vibrations associated with each axis as seen in Fig.2.5. ^{24}Mg is a bi-axially deformed nucleus and the ramifications of this K-splitting is discussed in later chapters.

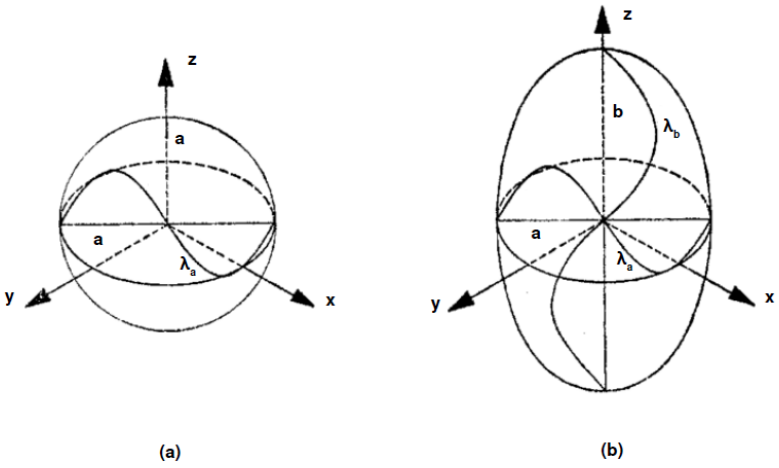

Figure 2.5: An illustration of the wavelength associated with a standing wave in a spherical nucleus (a) and the wavelength associated with a standing wave in nucleus (b). The wavelengths of the standing waves in nucleus (b) depend on the axis of vibration and the lower wavelength, (λ_b), has a higher associated energy than (λ_a) due to the de Broglie energy-frequency relation [34].

Giant Resonance Width and Decay

The second important property of a giant resonance is its width. The width is the property that determines the range of energy over which a GDR spans. It is determined by mainly three contributions.

$$\Gamma = \Gamma_{\uparrow} + \Gamma_{\downarrow} + \Delta\Gamma \tag{2.4}$$

The first arises because a GDR can be located above particle emission thresholds and particle emission contributes as a decay process. This contributes to the damping of the GDR and is known as the decay width $\Gamma_{\uparrow}$. Decay width is the dominant width for lower mass nuclei and can be determined from the relative population of 1p-1h states in the daughter nucleus. Decay to the ground state of the original nucleus by γ decay also contributes a small fraction of this decay width. The second contribution to the width of the GDR is called the spreading width, $\Gamma_{\downarrow}$, and arises from the coupling between 1p-1h states and 2p-2h states owing to the large densities of the 2p-2h states. The initial 1p-1h collective state mixes with 2p-2h states which then mix with 3p-3h states and so forth. This mixing continues until the energy of the excitation has been spread across all degrees of freedom and a compound nucleus is formed and the decay is then

governed by compound nucleus decay. The spreading width accounts for the largest portion of the width. The final contribution comes from the collective oscillations transitioning to non-collective excitations of the same multipolarity. This is known as Landau damping, $\Delta\Gamma$ [20]. The full width of the resonance is given by the sum of these widths as shown in the top panel of Fig: 2.6. A visualisation of how these different widths contribute can be seen in the bottom panel of Fig.2.6.

Since the giant resonances are relatively wide, up to a few MeV, they usually overlap significantly. This means that it can be difficult to distinguish between them. In the context of photoabsortion the three main resonances to consider are the ISGMR, IVGDR and the ISGQR. The measured strengths for the GRs in the energy range between 12 and 28 MeV are shown in Fig.2.7. The overlap is significant and, as shown in Fig.2.7, this presents an experimental problem when trying to study a single GR at a time. The strength of GR excitation is strongly dependent on the type of projectile used and its energy. This is also shown in Fig. 2.7, where the properties for each multipolarity were determined using different probes.

Previous Experiments Studying IVGDRs

Initially, experiments studying the IVGDR in light nuclei were mainly done using capture reactions and measuring the partial cross sections, (γ, xn), (γ, xp) or their inverse reactions, (n, γ), (p, γ) and combining this data with (γ, γ') data [40]. This method was not ideal as (γ, xn) can only probe energies above particle emission thresholds and (γ, γ') can only probe energies below particle thresholds without accurate branching ratio data for particle emission. Inelastic scattering of electrons was complicated due to excitation of isovector as well as isoscalar giant resonances and theoretical calculations had to be used to estimate the interference effects [41]. Coulomb excitation using heavy-ion beams at intermediate energies have been used to extract information on ground state γ decays and relativistic heavy ion beams have been used to investigate multiphonon excitations. Only with the advent of 0° detection systems such as the Grand Raiden at RCNP or the K600 at iThemba LABS, has virtual photon excitation using light probes become possible. This approach is ideal because it can gather high resolution data about the E1 response below and above particle emission equally well. The dominance of Coulomb interaction above nuclear interaction at 0° leads to almost negligible interference for between nuclear and coulombic interactions [42]. The theoretical details about this approach is highlighted in Section 2.2 and the experimental setup required to successfully conduct inelastic proton scattering at 0° is described in Chapter 3.

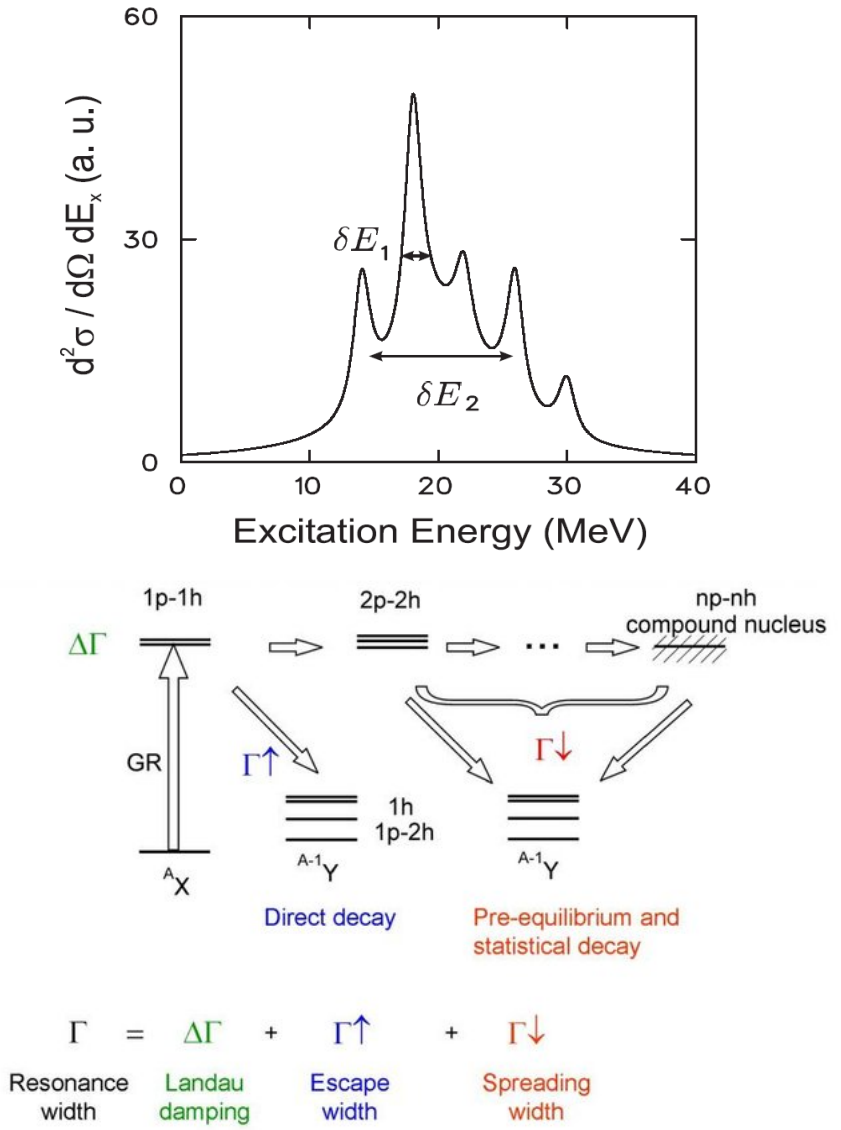

Figure 2.6: Top: The structure of the GDR width is composed of a superimposed mixture of widths of either narrow or broad energy peaks [35]. Bottom: The schematic representation of how the different decay mechanisms can contribute to the eventual width of a giant resonance [36].

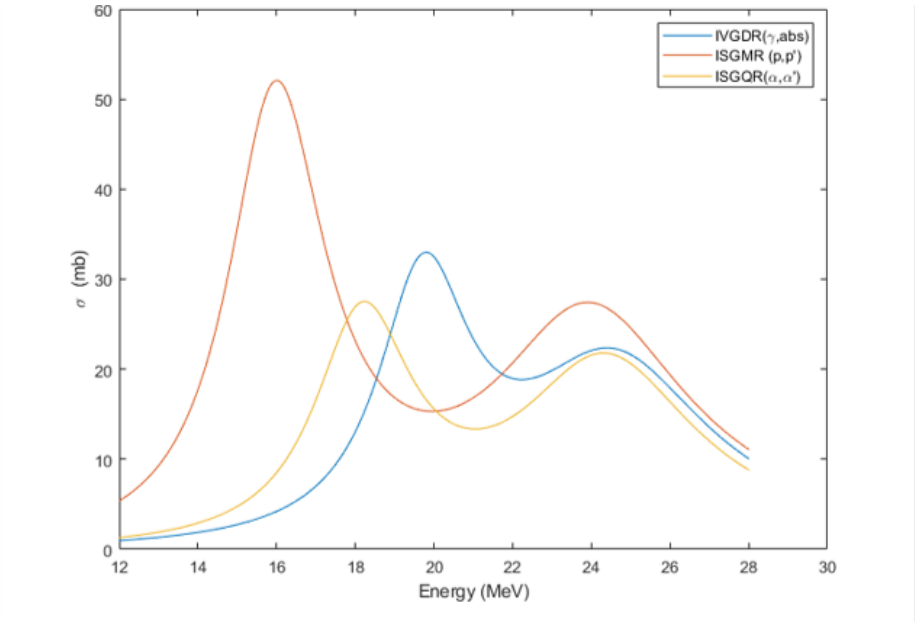

Figure 2.7: Graph showing the systematic calculations for positions of the ISGMR [37], IVGDR [38] and the ISGQR [39] in ^{24}Mg. The cross section depends on the type of probe but the positions and widths are independent of the type of probe used.

2.2 Photo-excitation

2.2.1 Coulomb Excitation

Coulomb excitation refers to excitation of a nucleus that is mediated by the electromagnetic force. The main concept to consider in this framework is that the projectile imparts enough energy to the target to leave it in an excited state without nuclear interaction. Assuming this excited state is bound, it has a finite lifetime after which a gamma decay to the ground state occurs. One of the pertinent visualisations of this process is to consider it as the exchange of virtual photons between target and projectile, a suggestion proposed by Fermi in 1933 [43]. With this technique the nucleus is excited without any nuclear interaction as the exchange of virtual photons allows the target to react with the projectile from beyond the reach of the shorter range nuclear force [44]. In the past, electrons were used for Coulomb excitation as the (e,e') reaction could excite E0 transitions that could not be reached via radiative capture nor by γ-absorption. The issue with exciting the IVGDR using electron scattering is that nearly all transitions are equally favoured and hence the selectivity of the probe is not ideal for such an experiment. The use of hadronic projectiles provide greater selectivity due to the scattering dependence on both isospin and spin. This allows a probe to be selected which will preferentially excite the giant resonance of interest as is the case with protons favouring the IVGDR excitation. Even with the added selectivity of protons as a projectile, the fact that they can excite natural and unnatural parity states can limit the value of this approach. At zero degrees scattering the favored mode for interaction is Coulomb excitation and E1 photons are the dominant multipolarity for virtual photon production [45]. The combination of these factors make relativistic zero-degree scattering experiments using protons a very viable reaction for investigating the IVGDR [46].

2.2.2 Classical Excitation

The original formulation of Coulomb scattering was made by Earnest Rutherford. This formulation described the trajectory based on the impact parameter, b, (the perpendicular distance between the path of approach and the target) and the scattering angle, θ, of an ion impinging on a nucleus. For a choice of impact parameter, b, larger than the sum of the radius of the target,vr_T, and the projectile, r_P , $b > r_T + r_P$, the strong force interaction becomes negligible compared to the electromagnetic interaction. The projectile in this description follows a hyperbolic arc as seen in Fig. 2.8 and the cross section has the following form [47]:

$$\frac{d\sigma_R}{d\Omega} = \left(\frac{Z_P Z_T e^2}{4\pi\epsilon_0 E}\right) \csc^4\left(\frac{\theta}{2}\right), \tag{2.5}$$

where Z_T and Z_P are the charges of the target and projectile.

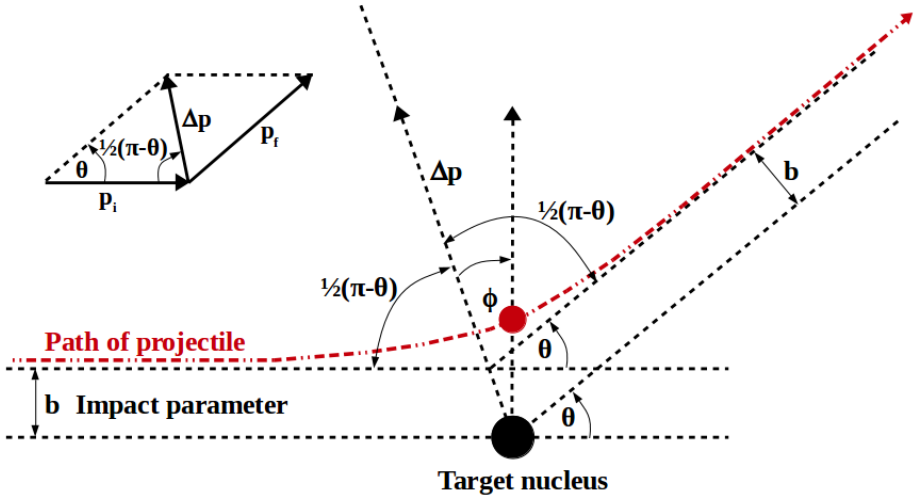

Figure 2.8: A schematic description of Rutherford scattering where the projectile follows a hyperbolic path [48]

2.2.3 Semi-Classical Excitation

Coulomb excitation is generally treated in a semi-classical manner where the scattering path is approximated to the Rutherford scattering trajectories while the differential cross section takes on a quantum mechanical form [28]:

$$\frac{d\sigma}{d\Omega} = \frac{d\sigma_R}{d\Omega} Q_{i->f}, \tag{2.6}$$

where Q represents the transition probability to excite the nucleus from the initial state, i, to the final state, f, and $\frac{d\sigma_R}{d\Omega}$ is the Rutherford cross section. During the approach and subsequent scattering, the target nucleus is subject to a time-dependent potential generated by the scattering particle, in this case protons, and it is assumed that the projectile is not excited [49].
In the context of the K600 spectrometer, the protons are accelerated to about 200 MeV and hence the projectile scattering is treated using a relativistic scheme [50]. This allows for the use of perturbation theory as long as the excitation is small compared to the energy scale of the system. Hence, the transition probability can be related to a scattering amplitude, $a_{i\to f}$ [28]:

$$Q_{i\to f} = |a_{i\to f}|^2. \tag{2.7}$$

It is a reasonable assumption that for Coulomb excitation the impact parameter is greater than the sum of the two nuclear radii and hence there is no overlap of charge distributions [42]. This means that the trajectory is largely unchanged

by interactions and that the potential $V(r(t))$ is purely electromagnetic. Thus, the scattering amplitude formula $a_{i\to f}$, in time-dependent perturbation theory becomes[28]:

$$a_{i\to f} = \frac{1}{i\hbar}\int_{-\infty}^{\infty} e^{i\omega t}\,\langle f|\,V(r(t))\,|i\rangle\,dt, \tag{2.8}$$

where ω represents the characteristic frequency of the system that is dependent on the initial, E_i, and final energies, E_f, of the system[28]:

$$\omega = \frac{(E_f - E_i)}{\hbar}. \tag{2.9}$$

The next step is to treat the potential, V, in terms of its multipole expansion which allows separation of the excitation amplitudes into electric and magnetic moments [28]:

$$a_{i\to f} = i\sum_{\lambda}\chi_{i\to f}^{\pi(\lambda)} f_\lambda(\zeta), \tag{2.10}$$

and

$$\chi_{i\to f}^{\pi(\lambda)} \simeq \frac{Z_p\,\langle f|\xi(\,{}^{E}_{M}\,)\lambda\mu|i\rangle}{\hbar\left(\frac{\nu}{c}\right)b^{\lambda}}, \tag{2.11}$$

where λ, σ and τ represent the multipolarity, spin and isospin of the excitation. The multipole expansion is given by $\xi(\,{}^{E}_{M}\,)$ which indicates that the excitation amplitude is expressed in terms of the expectation value matrix elements that correspond to electric and magnetic moments, $\xi(E\mu\lambda)$ and $\xi(M\mu\lambda)$. The projectile charge and speed are given by, Z_p and ν respectively. The adiabaticity of the system is represented by ζ and gives an indication of the timescale of the interaction relative to the energy of the reaction and depends on the velocity (ν) and impact parameter b[28]:

$$\zeta(b,\nu) = \omega\frac{b}{\nu\gamma}, \tag{2.12}$$

The adiabaticity for relativistic reactions where the excited state energy is small compared to the projectile energy, is approximated as unity $\zeta \approx 1$. This leads to a impact parameter of $b_a = \frac{\nu\gamma}{\omega}$. An estimate for projectile energies of 100-200 MeV/u gives impact parameters of between 10 fm and 20 fm [20]. The cross section of the final state can then be calculated using [28]:

$$\sigma_\lambda = 2\pi\int_{r_c}^{b_a} b|\chi_{i\to f}^{\pi\lambda}|^2 db. \tag{2.13}$$

Here the range of integration extends from the the radius of Coulomb excitation to the impact parameter b_a. This is the distance at which nuclear interactions are negligible. Substituting the perturbation equation 2.11 into the cross section equation 2.13 for a 0^+ ground state would yield the following [28]:

$$\sigma_{\pi\lambda} \approx \left(\frac{Z_p e^2}{\hbar c}\right)\frac{B(\pi\lambda; 0\to\lambda)}{e^2 r_c^{2\lambda}}\pi r_c^2 P(\lambda), \tag{2.14}$$

where:

$$P(\lambda) = (\lambda - 1)^{-1} \text{ when } \lambda \geq 2 \tag{2.15}$$

$$\text{and } P(\lambda) = (2ln(\frac{b_a}{r_c}))^{-1} \text{ when } \lambda = 1. \tag{2.16}$$

For the probing of a electric dipole resonance (E1), we have that $\lambda = 1$ and the reduced transition strength, B, for an E1 transition from a 0^+ ground state is given by $B(E1; 0 \rightarrow 1)$. Hence, equation 2.14 becomes [28]:

$$\sigma_{E1} = \frac{Z_p e^2}{\hbar c} \frac{(2ln(\frac{b_a}{r_c}))^{-1}}{e^2} B(E1; 0 \rightarrow 1). \tag{2.17}$$

2.2.4 Virtual Photons Excitation

A common method of calculating Coulomb excitation is the exchange of virtual photons. The concept that underpins this method is Fermi's theory of a virtual particle that mediates interactions between potentials. In this case the electromagnetic potential is substituted by the absorption of an equivalent amount of virtual photons in the target nucleus. This is done by taking a Fourier transformation of the electromagnetic potential and treating the result as a spectrum of virtual photons [50].

What follows is a brief summary of the method. For a more complete theoretical description refer to the review by Bertulani [50]. The calculation starts in a similar fashion to the cross section equation 2.13, where the reaction cross section is calculated using the interaction probability from a cutoff radius r_c to infinity:

$$\sigma_{\lambda\pi} = \int_{r_c}^{\infty} 2\pi b P(b) db, \tag{2.18}$$

Where:

$$P(b) = \int \frac{1}{E_\gamma} N_{\pi\lambda}(E_\gamma, b) \sigma_\gamma^{\pi\lambda}(E_\gamma) dE_\gamma, \tag{2.19}$$

$P(b)$ is the probability that a relativistic electromagnetic interaction occurs. This quantity depends on the photonuclear cross section, $\sigma_\gamma^{\lambda\pi}$, and the number of virtual photons, $N_{\pi\lambda}$, incident on the target nucleus per unit area. These photons are of energy $E_\gamma = \hbar\omega$ and are constrained to be produced at the impact parameter.
The radius r_c is the low cutoff parameter and it indicates the maximum range at which virtual photons are produced. It is always greater than the sum of the two nuclear radii $r_T + r_P$ due to the addition of the Coulomb excitation radius r_{CE} [28]:

$$r_c = r_T + r_P + r_{CE}. \tag{2.20}$$

The total number of virtual photons produced for an E1 transition becomes:

$$N_{E1}(E_\gamma) = \frac{2Z_p^2\alpha}{\pi}(\frac{c}{\nu})^2[\zeta K_0 K_1 - \frac{2Z_p^2\alpha}{2c^2}(K_1^2 - K_0^2)], \tag{2.21}$$

and the amount of virtual photons produced per solid angle becomes:

$$\frac{dN_{E1}}{d\Omega} = \frac{Z_p^2\alpha}{4\pi^2}\zeta^2\epsilon^4\frac{c^2}{\gamma\nu}[K_1^2(d) + \frac{1}{\gamma^2}K_0^2(d)], \tag{2.22}$$

where, α, is the fine structure constant, ν is the projectile speed in natural units, γ, is the Lorentz factor and the adiabaticity parameter is based on half the distance of closest approach with a reduced mass. The eccentricity is the same as normally reported in scattering equations $\epsilon = \frac{1}{sin(\frac{\theta}{2})}$:

$$\zeta = \frac{\omega}{\nu}\frac{Z_p Z_t e^2}{m_0 v^2}. \tag{2.23}$$

In this case α is the fine structure constant and the functions K_1 and K_0 are modified Bessel functions. The double differential cross section is what is measured experimentally and is related to the photoabsorption cross section in the following way:

$$\frac{d^2\sigma}{d\Omega dE_\gamma} = \frac{1}{E_\gamma}\frac{dN_{E1}\sigma_\gamma^{\pi\lambda}}{d\Omega}(E_\gamma). \tag{2.24}$$

Eikonal Approximation

In this experiment the Eikonal approximation was adopted to calculate the number of virtual photons generated [51]. This was used because a normal virtual photon calculation in a semiclassical approximation has a pole at zero degrees and as such it will not produce valid results for this zero-degree experiment. The Eikonal model was developed to compensate for this and accounts for a more physical scattering situation that includes absorption and relativity. A more complete description of the approach is given in [33].
The amount of virtual photons produced for each multipolarity in the Eikonal model is given by:

$$N_{\pi\gamma} = Z_p^2\alpha\frac{\lambda[(2\lambda+1)!!]^2}{(2\pi)^3(\lambda+1)}\sum_m |G\pi\lambda m|^2((\frac{c}{\nu})g_m(\omega). \tag{2.25}$$

The $|G\pi\lambda m|^2$ factor is related to the Gegenbauer polynomial [52] and for the relevant case ($L = 1$) has the analytic solution for a variable x:

$$G_{E10}(x) = -i\frac{4}{3}\sqrt{\pi(x^2-1)}, \tag{2.26}$$

and the factor $g_m(\omega)$ is:

$$g_m(\omega) = 2\pi(\frac{\omega}{\gamma\nu})\int bK_m^2(\frac{\omega b}{\gamma\nu})exp(-2\chi_I(b))db, \tag{2.27}$$

where χ_I is the imaginary part of the function χ, given by:

$$\chi(b) = -\frac{1}{\hbar\nu}\int_o^\infty U_N^{opt}(z', b)dz' + \phi_c(b). \tag{2.28}$$

The optical nuclear potential U_N^{opt} is required and it is obtained using fits to elastic-scattering data. The second term ϕ_C is the Coulomb phase and is cast as follows:

$$\phi_C = 2\frac{Z_p Z_T e^2}{\hbar\nu}(ln(kb) + \frac{1}{2}E_1(\frac{b^2}{R_G^2})), \tag{2.29}$$

here R_G is described by the Gaussian radii of the nucleus and $E1$ is given by:

$$E_1 = \int_x^\infty \frac{e^{-t}}{t}dt. \tag{2.30}$$

The number of virtual photons produced per multipolarity as a function of projectile energy in the Eikonal model is given by:

$$\frac{dN_{\lambda\pi}}{d\Omega} = Z_p^2\alpha\frac{\omega k}{(\gamma\nu)}^2\frac{\lambda[2\lambda+1!!]}{(2\pi)^3(\lambda+1)}\sum_m |G_{\pi\lambda m}|^2|\Omega_m(q)|^2, \tag{2.31}$$

where the function $\Omega_m(q)$ is determined by the momentum transfer, q, and spin transfer $J_m(qb)$:

$$\Omega_m(q) = \int_0^\infty bJ_m(qb)\left(\frac{\omega b}{\gamma\nu}\right)exp(i\chi(b))db. \tag{2.32}$$

The key difference in these approaches is highlighted by Fig. 2.9. It shows the asymptotic behaviour of the semi-classical approach at small angles and how this pole is addressed by the Eikonal approximation.
The equivalent photoabsorption cross section can be obtained using:

$$\frac{d^2\sigma}{d\Omega dE_\gamma} = \frac{1}{E_\gamma}\frac{dN_{E1}\sigma_\gamma^{\pi\lambda}}{d\Omega}(E_\gamma). \tag{2.33}$$

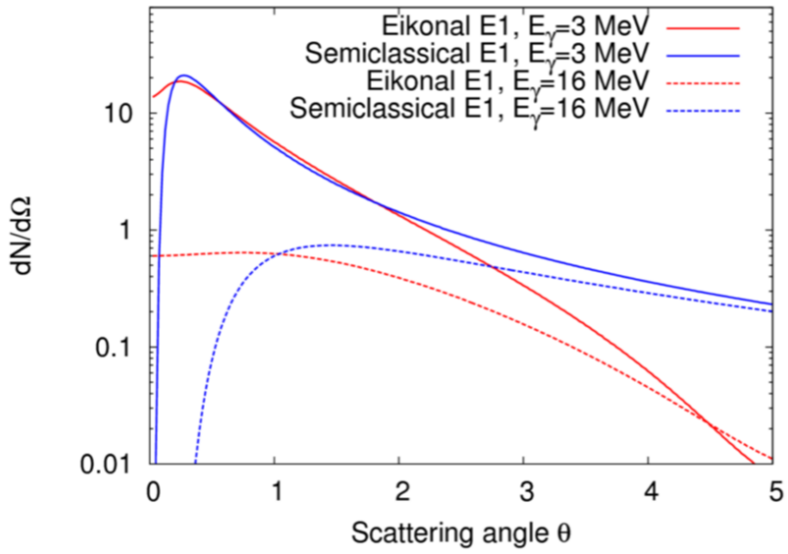

Figure 2.9: Comparison between the Eikonal model and the semiclassical model virtual photons per unit solid angle for 296 MeV protons incident on a ^{154}Sm target at different scattering angles (degrees).[53]

Chapter 3

Experimental Setup

The iThemba Laboratory for Accelerator Based Sciences facility (iThemba LABS) is situated near Cape Town, South Africa. The data used for the extraction of the photoabsorption cross section of ^{24}Mg is part of the PR210 experiment at the iThemba LABS. The K600 magnetic spectrometer in a zero degree measurement configuration is used to analyse the scattering of the dispersion matched proton beam generated by the Separated Sector Cyclotron (SSC). This section focuses on the experimental setup and its specifications.

3.1 iThemba LABS facility

In Fig. 3.1 the layout of the different beamlines that are used for experiments at iThemba LABS can be seen. The solid pole injector cyclotrons (SPC1 and SPC2) have a K value of 8 and are used to accelerate and inject ions produced by either the Penning Ionization Gauge (PIG) or the Electron Cyclotron Resonance ion source (ECR) into the main SSC:

$$K = \frac{mE}{q^2}, \tag{3.1}$$

where m is the mass in amu, E is the energy of the beam and q is charge of the projectile. For this experiment protons are made using the ECR by separating ^{2}H using a radio frequency (RF) resonance. Separated protons are then injected into SCP2 from which they are transported via beamline J into the K=200 SSC. The protons are then accelerated to the required 200 MeV and sent to the K600 magnetic spectrometer using lines X, P1, P2 and S. These lines are equipped with quadrupole and dipole magnets and have slits to help reduce the beam spread as the protons traverse the beamline.

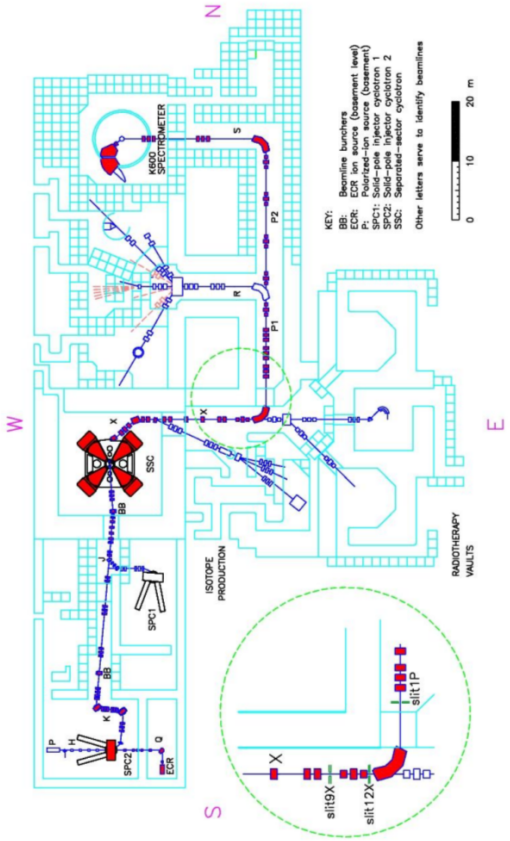

Figure 3.1: A schematic representation of the iThemba LABS SSC facility. The main beamlines are shown along with the various beam splits towards different detectors/experiments [54].

3.2 The K600 spectrometer

The working principal of the K600 is based on the magnetic rigidity of a charged particle travelling in a magnetic field. The deflective force that the particle experiences in the magnetic field is related to its momentum. Energy loss caused by interactions with a target causes a particle to deflect more and thus be separated by the spectrometer. In Fig. 3.2 the red and green lines represent the trajectories of the unscattered beam particles and the one subject to reaction with the target nuclei, respectively. To achieve momentum separation, the K600 is built up of 3 different bending magnets, a quadrupole and two dipoles, and a set of trim coils. The quadrupole magnet is used for vertically and horizontally focusing the particles at the entrance of the spectrometer and the dipoles for beam spot adjustments. The ratio of the fields of the bending dipoles can be adjusted in strength to allow for three different dispersion strengths: low, medium and high dispersion. These effects are shown in Fig. 3.2 where the radius of curvature of the interacting particles can be made to impinge on either the high, medium or low dispersion planes. The trim coils are the final focusing component of the K600 and serve to correct different orders of kinetic aberrations. The K-coil is triangular and thus corrects for first order variations using a dipole and quadrupole field whereas the H-coil uses a dipole and hexapole component to compensate for second-order aberrations.

3.2.1 Focal Plane Detection Suite

In order to deduce the information regarding the particles' trajectories and energies, a composite detection system is placed at the selected K600 focal plane. For the experiment described in this dissertation the focal plane detection system was composed by two vertical drift chambers and two plastic scintillators as depicted in Fig.3.3. In the following sections details on the different components are given.

Plastic Scintillation Detectors

These detectors are sometimes referred to as the paddle detectors due to their long, flat geometry. They consist of two Bicron-BC408 102 cm $\times$ 10.2 cm boards that are covered in aluminised mylar which ensures that they are light tight. The plastic scintillators are connected via light guides to photomultiplier tubes at the ends of each scintillator and this allows for these detectors to measure coincidence between them. The plastic scintillators are used for trigger generation and particle identification through energy difference spectra. For the run of this experiment the voltage of the photomultiplier tubes in the scintillating detectors were set to -1900V.

Vertical Drift Chambers (VDC)

The VDCs are the primary tool for accurate position and angle determination of an event. The drift chamber is situated in front of the scintillation detectors

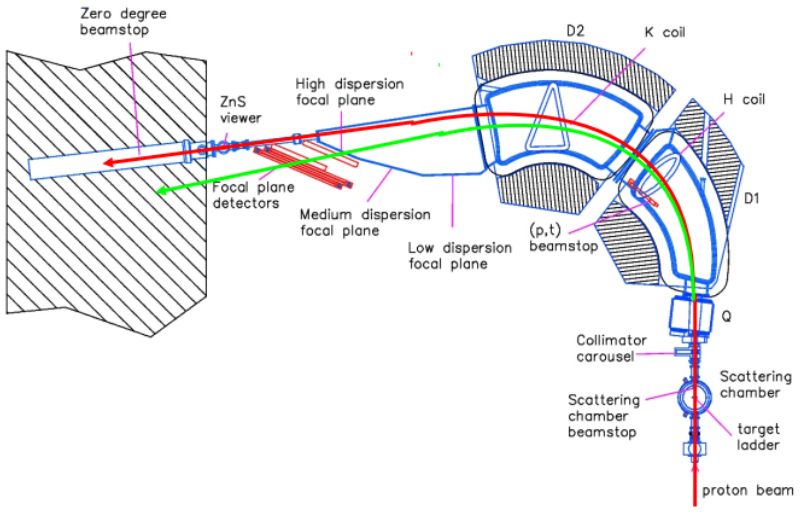

Figure 3.2: The schematic zero-degree configuration of the K600 spectrometer showing the undispersed beam (red) and the dispersed beam (green). The beam enters from the bottom and moves from right to left through the spectrometer.[54]

Table 3.1: The technical specifications of the focal plane detectors used in this experiment [54].

New X&U Vertical Drift Chamber	
Wire configuration	vertical and 50°
Horizontal VDC acceptance	78 cm
Vertical VDC acceptance	10 cm
Signal wire	20μm gold plated tungsten
Guard wire	50μm gold plated tungsten
Cathode planes	20μm Al foil
Number of signal wires	198 and 143
Number of guard wires	201 (=199+2) and 146 (=144+2)
Cathode-anode spacing	8 mm
Signal wire spacing	4 mm
Guard wire spacing	4 mm
Gas mixture	90% Ar 10% CO_2
Entrance and exit windows	25μm mylar
Pre-amplifier	Lecroy 2735 (13 units)
Typical guard wire voltage	$\sim$ -500 V
Typical cathode plane voltage	$\sim$ -3800 V
Paddles	
Scintillating material	Bicron BC-408
Scintillator dimensions	48 $\times$ 4 $\times$ 0.5 (or 0.25) inch^3
-	= 1219.2 $\times$ 101.6 $\times$ 12.7 (or 6.4) mm^3
Lightguide	Saint Gobain Crystals 90° adiabatic twisted pair
PMT	Hamamatsu R329-02 PMT tube with a Hamamatsu E934 base
Typical PMT voltage for 200 MeV protons	$\sim$ -1700V for 0.5 inch $\sim$ -1900V for 0.25 inch
Max PMT voltage	2700V

as shown in Fig. 3.3. The VDCs are setup in a configuration characterised by two wire planes: The X-wire plane made of wires perpendicular to the focal plane and the U-wire plane with wires angled at 50^0 to the focal plane. The wire planes contain 198 gold-plated tungsten signal wires each 20 microns in diameter and spaced 4mm apart which generate an electric field to guide the ionised electrons to the anodes. The signal wires are staggered with 199 field shaping wires that are 50 microns thick. These field shaping wires are sometimes referred to as guard wires and carry a negative voltage of 500V. Three aluminium cathode planes used for charge extraction sandwich the wire-planes and a typical voltage of +3700V is applied for 200 MeV proton detection. The wires are separated from the atmosphere by a thin layer of a 10% carbon dioxide and 90% argon gas mixture kept in mylar sheets between them. The full specifications of the detector suite is given in Table 3.1.

During a run, positively charged ions impinge on the detector and cause ionisation of the argon gas in a track throughout the detector. The electrons that are generated then drift to the anode signal wires and charge multiplication occurs when they are close to the signal wires. The guard wires help to shape the field generated by the signal wires to have a more linear and uniform be-

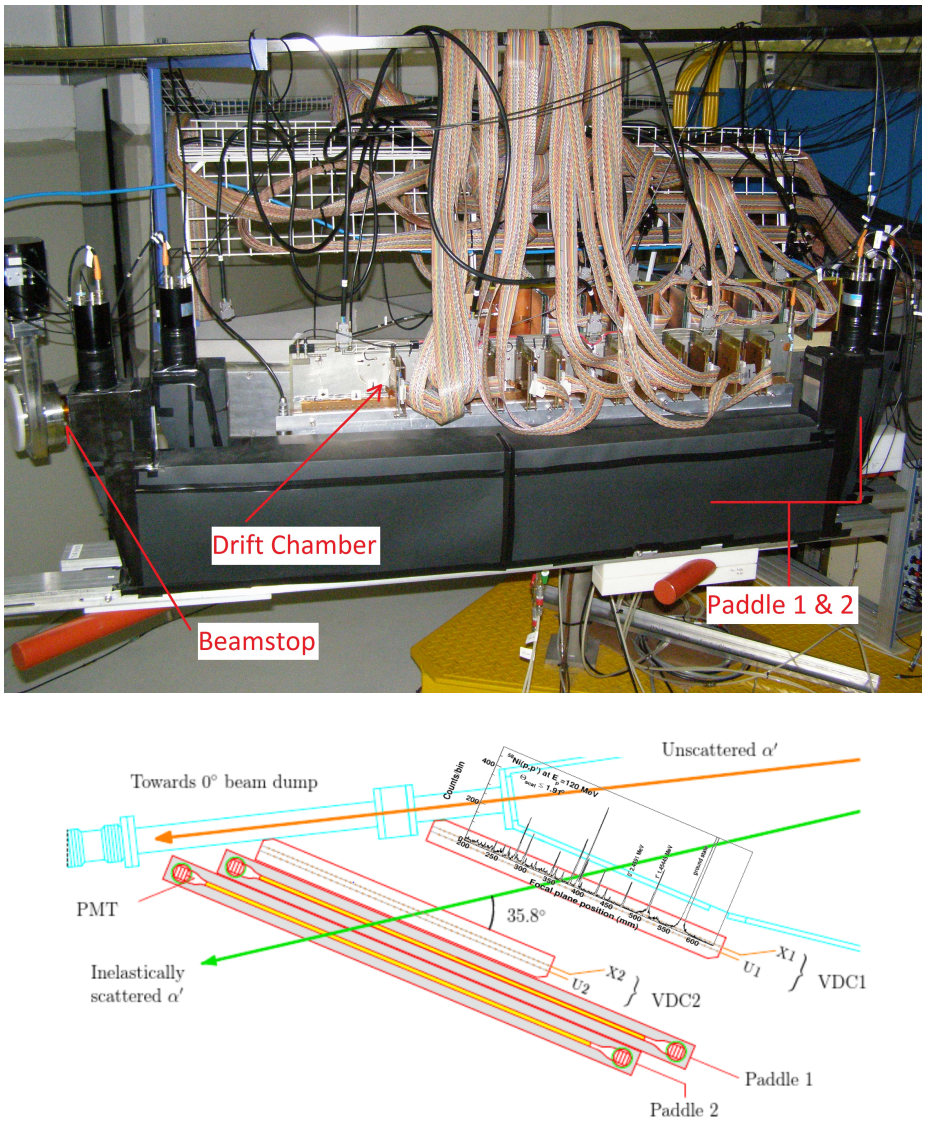

Figure 3.3: Top: Photo taken of the focal plane detection package showing the plastic scintillators detectors and paddle VDCs. Bottom: A schematic representation of the focal plane detection suite's layout. It shows an example of the relative focal plane position overlaid on top of VDC 1 and the scattering path of a unscattered (orange) and inelastically scattered projectile (green) [55].

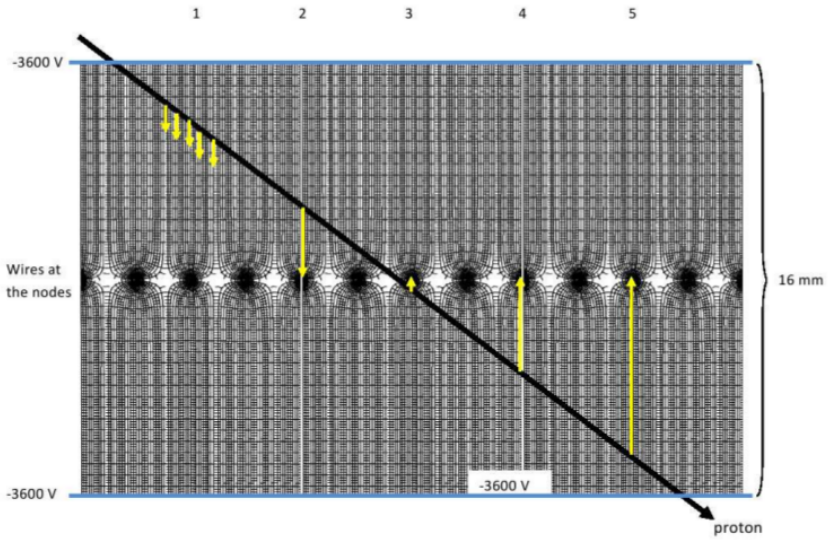

Figure 3.4: A Garfield calculation of the VDC field lines and a hypothetical proton track moving through it. In this case, the field lines show that wires 1-5 are active and the drift times for these ionisations will result in a single pulse [54].

haviour throughout the detector. Two larger guard wires are placed at each end of the detector to preserve the uniformity of the field and prevent unexpected discharges. The drift times of the electrons in a field cell is then measured and used to create an event. Fig. 3.4 shows a hypothetical event of a proton impinging on a drift cell where the gas is ionized along the particle track. Each of the ions then drift towards the anodes along the electric field lines. The drift times go from long drift times upon entering the cell to shorter drift times as it crosses the signal wires and then long drift times as it exists the cell. In a "good" event the drift time T_d on each side of the drift wire would be given by:

$$T_d = \pm(a - ti), \tag{3.2}$$

where t_i is the raw drift time from the time to digital converters (TDC). Each drift time is offset by a time a after all the pulses from the wires have arrived. The drift time becomes more non-linear for shorter drift times as a larger fraction of their total drift time is on curved field lines. This leads to the shortest drift times usually being discarded. From these values it is possible to determine the particle track from the drift times using a look up table method described in Chapter 4. It is important to note that each of the cable channels require offsets relating to the cable-length of the preamplifier to the TDC, the path in the preamplifier and the path length of the track to the preamplifier and the

prescription for dealing with this is also discussed in Chapter 4. Anomalous events such as a particle only clipping the top of a drift cell can introduce disturbances in the drift times and these events are generally discarded by a trigger veto. A typical spectrum of event times for a single run of an experiment is given in Fig. 3.5.

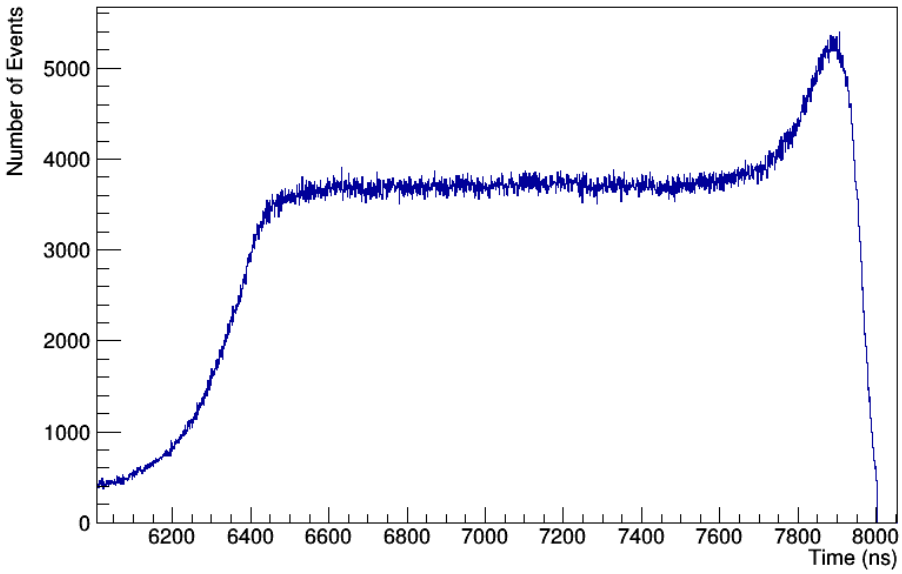

Figure 3.5: A drift time spectrum of the accepted events in a run. The lower end of the spectrum corresponds to events that passed through the edge of the drift cell whereas the longer drift times are related to particles that pass through the entire drift cell.

3.2.2 Data Acquisition System

The data acquisition (DAQ) system used during K600 experiments is a combination of Time to Digital converters (TDC), charge to digital (QDC) converters and a signal analyser known as the Maximum Integrated Data Acquisition System (MIDAS) [56]. The wire-planes register signals which, after preamplification and discrimination, are sent to P-TM 005 16-channel electronic cards. The signals then get transported via twisted pair-ribbon cables to the CAEN V1190A TDCs which interpret and convert the signals into time measurements at a time resolution of 100 ps. The plastic scintillators detectors and photomultiplier tubes are connected to the CAEN V792 QDC. A quadruple coincidence between the four photomultiplier tubes in the two plastic scintillators detectors sends a trigger signal to the MIDAS system which is then used to gen-

erate an event. The electronics used in this setup have an inherent analysing time associated with each component. The time it takes for the system to process an entire event is called the resolving time of the system. Two events cannot be simultaneously analysed and this leads a fraction of events that are counted but not processed. In the case of the K600 this system is managed by a dual event counter and a veto system. When a event is recorded the DAQ increases the counts of both the inhibited and uninhibited event counters. If an event occurs while the electronics are still processing a previous event, a veto trigger adds the incoming event signal to the uninhibited scaler counter only. The dead time of the DAQ is measured as the fraction of events present in the uninhibited counter but not in the inhibited counter. The complete layout of the electronics used in the K600 system is shown in Fig.3.6.

3.2.3 Target Carousel

The target ladder for the experiment PR210 was set up in the following way: ^{42}Ca, ^{44}Ca, ^{48}Ca, ^{24}Mg, empty and Mylar as shown in Fig. 3.7. The ^{42}Ca and ^{44}Ca target were for used other experiments but they proved useful as a white spectrum for the look up table generation and cable length calculation as discussed in Chapter 4.2. The empty slot was used for identifying beam related background and particle identification discussed in sections 4.1 and 4.4. The target of interest, ^{24}Mg, was produced by hot rolling a pure metal under an argon atmosphere to the desired thickness of 2μ m and areal density of 2.1 mg/cm^2. The ^{24}Mg is self supported in the target frame.

3.2.4 Zero Degree Mode

Many nuclear reactions have a much higher reaction rate when performed at angles approaching zero degrees, in particular excitations which require low momentum transfer. In the case of this experiment an angular momentum transfer of L=1 is being investigated, making a zero-degree scattering experiment ideal. Nuclear reactions at zero-degree scattering angles have been notoriously challenging to properly implement due to the difficulty of separating the main beam from the scattered beam. One of the factors that limit the effectiveness of these experiments is usually the beam halo. This refers to the beam-related background of particles that have different phase-space coordinates than that of the main beam causing an effect visually similar to that of a halo. It is imperative that the beam has a small halo to help reduce the amount of background that detection system receives since the unreacted beam passes just 10 cm from the focal plane detectors. To perform these experiments at iThemba LABS, the focal plane detectors need to be positioned in the high-dispersion mode as seen in Fig. 3.2. After the beam has passed through the focal plane it is guided into a beam dump as seen in Fig. 3.2. The zero-degree beam dump consists of a Faraday cup placed into the concrete wall. Further down the beamline there is also a scintillating viewer. This viewer is mainly used to optimize the traversal

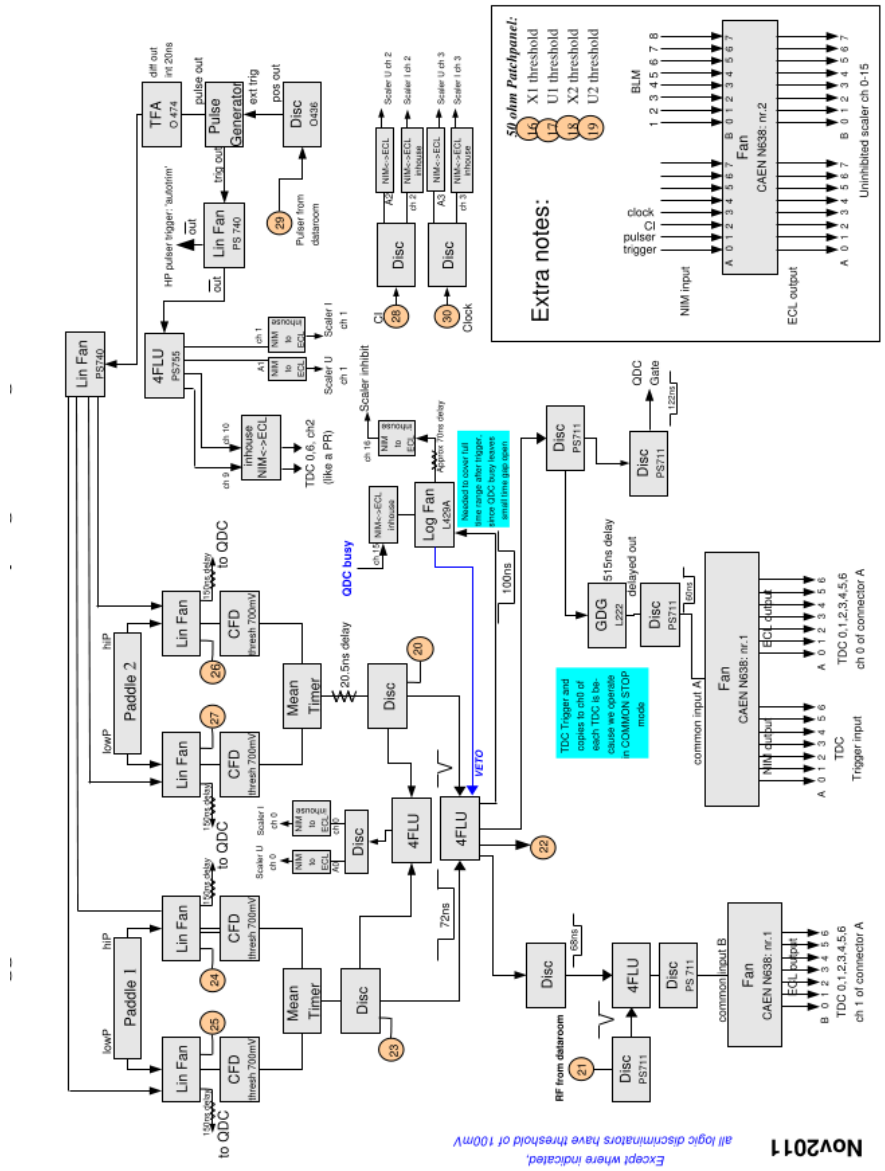

Figure 3.6: A typical layout of the trigger electronics used in K600 experiments.[54]

Figure 3.7: The target ladder used in the PR210 experiment [55].

of the beam through the spectrometer and an example of a scintillation viewer is the Hatanaka mesh seen in Fig.3.8.

3.3 Experimental Procedure

The experiment is performed at a zero-degree scattering angle. The requirements for zero-degree scattering at high energy resolution to be consistent are stringent in comparison to other experiments. A small energy spread on the beam, a faint halo and small emittance are essential to the success of the Zero-degree mode measurement. The stability of the beam over the course of the experiment is also vital to the execution of the experiment.

3.3.1 Halo Optimization

As mentioned in the zero-degree section earlier, the success of experiments at such small scattering angles depend largely upon the elimination of background related to the unreacted beam. This background consists of target and beam backgrounds which have to be dealt with separately. The beam background is minimized during the beam tuning whereas the target related background is addressed during analysis and is discussed in Section 4.4.1.

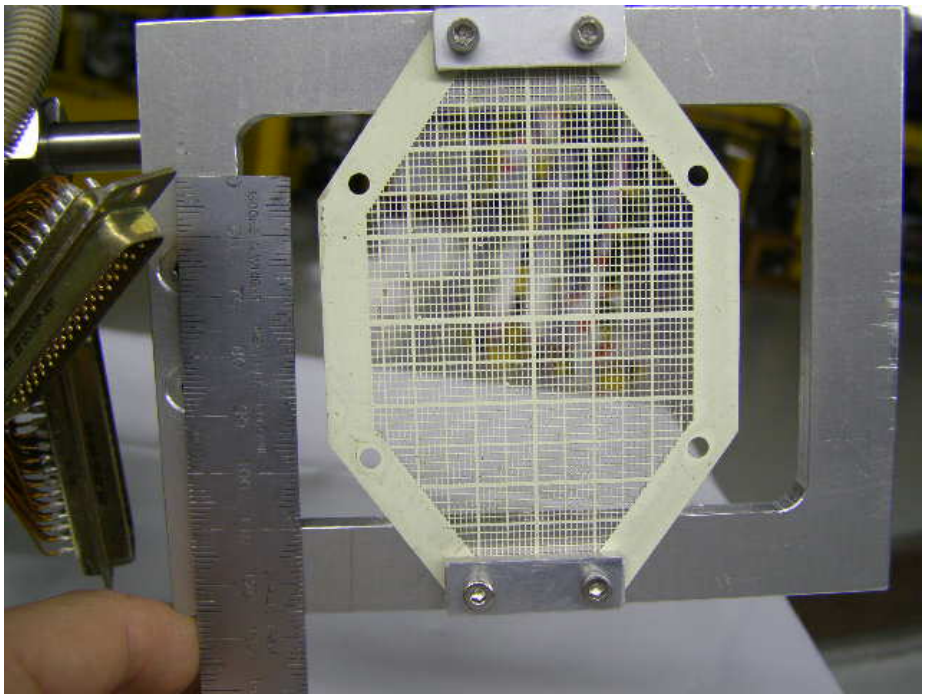

Figure 3.8: The 45° beam viewer known as the Hatanaka mesh [57].

Following injection into the SSC, the beam divergence and spread is controlled using a series of slits downstream in the beamline. An unfortunate side effect of these slits is that a halo is induced and an already reduced beam is further diminished (about 5% of the protons injected into the SCC makes it to the spectrometer [58]). To reduce the amount of beam halo that arrives at the spectrometer a series of 90-degree bending magnets are employed in conjunction with 4 clean-up slits. In addition to that, the amount of potential scattering sites inside the beamline has been reduced by increasing the size of the beamline in these crucial zones. As an additional step towards reducing scattering in a high dispersion experiment, the low dispersion edge of the target frame was removed as shown in Fig. 3.9.

3.3.2 Dispersion Matching

Dispersion matching is a method by which the energy resolution of the beam energy can be bypassed and much more sensitive resolution of the spectrometer can be used. In essence it relates to matching the focal plane measurement to the beam at the target location. The K600 is only capable of achieving lateral and focused matching at zero degrees as angular dispersion matching is only possible when running the beam in off-focus mode. An important assumption

Figure 3.9: A photo showing the target frame used in the PR210 experiment. The lower dispersion sides of the frame has been removed to reduce the amount of scattering from it [54].

in the case of dispersion matching is that the nuclear reaction is not sensitive to the inherent energy spread of the beam itself. In the case of 200 MeV protons impinging on ^{24}Mg at iThemba LABS this assumption is realistic. The first step of dispersion matching is to apply kinematic corrections to the initial beam.

Kinematic Corrections

The initial kinematic corrections that are employed ensure that a strong nuclear state has upright convergence in the focal plane position-angle spectrum. This means particles excited from the same state with different focal plane angles, θ_{fp}, all focus onto a single horizontal position, x_{fp}. This is done by implementing changes in the K-coil for linear corrections, θ_{fp}, and the H-Coil for quadratic adjustment, θ^2_{fp}. Kinematic corrections alter the ion-optical character of the beam and should be implemented before changes requiring a constant beam ion-optic character such as the faint beam and other matching methods. Further kinematic corrections are also employed offline during the analysis and this is discussed in Section 4.3.3.

Lateral and Focus matching

Standard starting procedure for a non-dispersion matched beam is to set up a double achromatic transport. This means that the spatial coordinates, position and angle, are independent of the momentum of the incident proton. The resolution that can be obtained from such a beam is given by the inherent distribution of the beams momentum rather than the resolution of the spectrometer. To compensate for this the protons are spatially separated according to their momenta. This means that lower momenta protons will travel a shorter distance through the spectrometer than higher momentum protons as seen in the leftmost panel of Fig. 3.10. This level of dispersion matching is known as an effective achromatic focus [59]. This is the most basic level of dispersion matching and it can only be effective when the beam width is precisely calibrated. The spectrum obtained from only focus matching results in a good energy-resolution excitation energy spectrum but not a high energy-resolution absolute energy spectrum.

Lateral matching is the process of matching the spatial coordinates of the same energy interactions to the same horizontal position coordinate on the focal plane thus offsetting the dispersion of the beam. This involves adjusting the magnetic field so that the shorter paths bend slightly less than the longer paths as seen in the central panel of Fig. 3.10. This does introduce some angular ambiguity in the measurements but produces a focal plane distribution with tighter position and angle groupings and thus higher resolution. The magnets' strength values obtained during the dispersion matching for this experiment are given in Table: 3.2.
Angular dispersion matching is not relevant to this experiment as the K600 cannot be run in the vertical off-focus mode required to implement it for the zero-

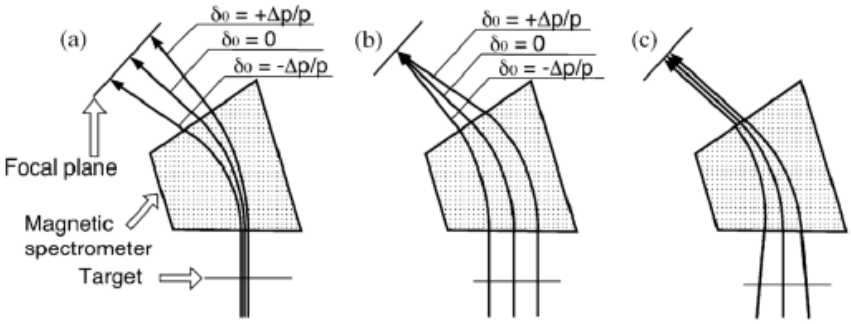

Figure 3.10: A representation of charged particle paths under different dispersion matching conditions. (a) Achromatic focused matching of the beam is achieved; (b) Lateral dispersion matching and focused matching is achieved; (c) Lateral and Angular dispersion matching is achieved [59].

degree configuration. If angular matching is successfully achieved, the angular ambiguity introduced by lateral matching can be eliminated.
A more mathematical description of dispersion matching can be examined using transport coefficients. These coefficients connect the traversal of the beam from the target to the focal plane and the minimization of angular and spatial matrix elements correspond to the process of dispersion matching described above. For a more detailed discussion regarding transport matrices refer to [60].

Table 3.2: The dispersion matching settings of the K600 spectrometer for high dispersion, 200 MeV protons.

Magnet	Magnet Current Strength (A)
Q	-467.801
D1	422.820
H	-60.522
D2	290.717
K	20.644

3.3.3 Faint Beam Method

Finite angle experiments generally use the ground state of a calibration target in order to determine the matching conditions for the focal plane. At 0°, the detected energy spectrum for 200 MeV protons starts at close to 8 MeV and this renders ground state calibration impossible. Instead, a beam entering directly into the K600 at 0° can be used to determine the matching conditions for the focal plane. However, detectors such as the VDCs and the plastic scintillator

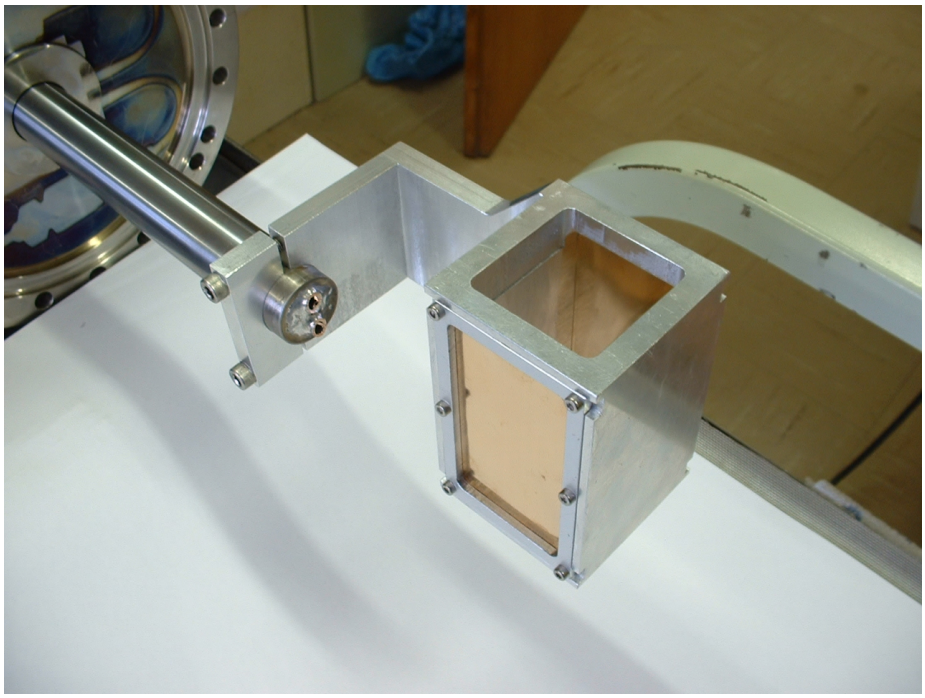

Figure 3.11: Meshes that retain the ion-optic characteristics of the beam but reduce the beam intensity by a factor of 10000.

detectors are not designed to handle direct beam currents in excess of 1 nA and will likely be damaged. In order to bypass this constraint, the faint beam method for dispersion matching was developed. The faint beam method refers to using a reduced beam intensity to directly view the beam without altering the ion-optical properties of the beam in order to ensure that the dispersion matching is optimised and the beam quality is adequate. This was performed by overlaying attenuation meshes downstream in the beamline, each reducing the current by a factor of 10, 100 or 1000. One such combination is shown in Fig. 3.11 where a mesh of factor 1000 intensity reduction is placed in front of a factor 10 intensity reduction mesh for a combined reduction factor of 10000.

Chapter 4

Data Analysis

This chapter focuses on how the data was obtained and then analysed offline from MIDAS [56] files using ROOT software [61]. The scripts used were written in C and C++ and in some cases Python, MATLAB and Microsoft Excel.

4.1 Data Extraction

4.1.1 PID (Particle Identification)

The magnetic setting of the K600 can be used to measure two quantities directly, the magnetic rigidity and, from that, the momentum, p, of a particle of known charge, q, can be determined. This is done by measuring the radius of curvature of the particle in the K600 bending magnets:

$$R = rB = \frac{p}{q}, \tag{4.1}$$

where R is the magnetic rigidity and B is the magnetic field.

The radius of curvature through the spectrometer is related to the path length that a particle travels in the spectrometer. Particles with similar momenta but different rigidities have different travel times in the spectrometer. The Time of Flight (ToF) method uses this difference and the energy deposition in the plastic scintillator detectors for PID. The relative ToF spectrum is generated by using a TDC to digitise the time interval between a plastic scintillator coincidence signal and the SSC RF (Radio Frequency) signal.
Fig.4.1 shows the 2-D spectrum of ToF vs energy deposited in the first of the plastic scintillators for an empty run (top panel) and for a ^{24}Mg run (bottom panel). There are two main lobes of particles present in the ^{24}Mg ΔE versus time of flight spectrum. The distinct lack of events in the bottom left lobe of the empty panel clearly indicates that the section between 5060 ns and 5100

ns is related to the proton that scatter off of the target and the remainder of the events are background events. To isolate the background from the signal region a graphical gate indicated by the solid black line in Fig. 4.1 is applied. This ensures that inelastically scattered protons are the selected events used for further analysis.

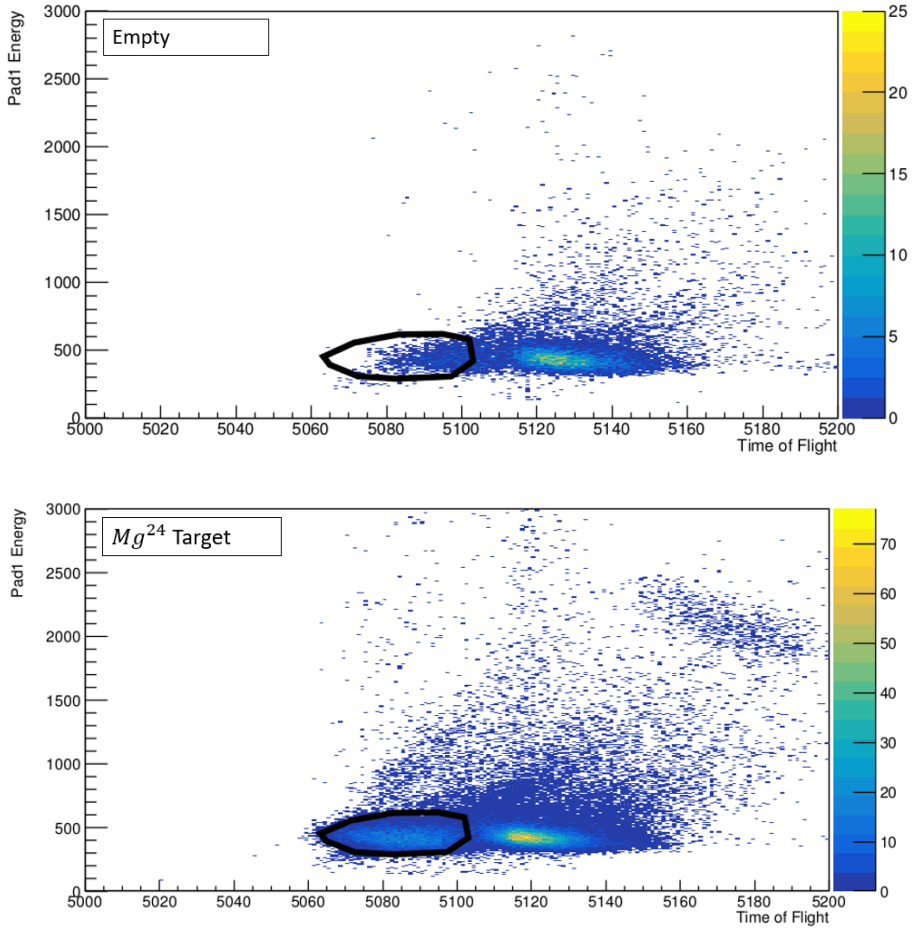

Figure 4.1: 2D matrix representing the ToF vs energy deposition for a run with an empty target (top panel) and the ^{24}Mg target (bottom panel). The PID graphical cut to select the inelastically scattered protons is shown with a solid black line in both panels.

4.1.2 Cable Length Offsets

The ribbon cables used between the preamplifier and the TDC have different lengths and internal circuit lengths which introduce variations in drift times.

To amend this, an offset is introduced to each TDC channel to synchronise the measured times of each event in the software. In general it is favorable to use a target that produces a uniformly illuminated, structure-less spectrum to ensure that each wire is evenly activated.
The cable length offsets are generated using a C++ script that determines the minimum gradient of the peak on the short drift time side of the drift time spectrum for each individual channel, and calculates the necessary offset parameter relative to a predetermined parameter t_{corr}. After generating the offsets with the code, minor adjustments need to be made to optimise some individual channels. The effect of this correction is shown in the correct lining up of the drift time edges from Fig. 4.2. After these offsets are applied a look up table is generated which converts the time information into focal plane locations.

4.1.3 Look Up Tables (LUT)

The drift time spectrum for the good events in a run are shown in Fig. 3.5, a description of what classifies as a good event is discussed in Section 4.4.4. The lower end of the spectrum for drift times less than 6500ns correspond to particles that only partially pass through the wire plane. This leads to short drift times but also limits the amount of ionisations per unit time. The opposite is true at the upper end of the spectrum above 7700 ns, where the amount of ionisation per unit time is large but the drift time is longer.
In order to transform the time signal from a detector into a focal plane position, the drift-time characteristics of the detector need to be established. The drift time distribution $\frac{dN}{dt}$ can be used to determine the distance, y, from the signal wire to the drift cell that a particle crossed through:

$$y(t) = \frac{dy}{dN} \int_t^{t_0} \frac{dN}{dt'} dt', \tag{4.2}$$

where the integral limits are from the time a particle arrives at the drift cell, t, to the time the pulse appears at the anode, t_0. A characteristic drift-time distribution is obtained by uniformly illuminating the focal plane and measuring the timing response of the signal wires against the constant value of $\frac{dN}{dt}$. The drift velocities can then be determined, which gives the focal plane position of events:

$$y(t) = \int_t^{t_0} \omega(t') \propto \int_t^{t_0} \frac{dN}{dt'} dt. \tag{4.3}$$

For this experiment, a (p, p') spectrum of ^{42}Ca was used. In general, there are cases where the LUT needs a slight adjustment due to the non-linear geometry of the electric field generated by the signal and guard wires. Fig. 4.3 shows drift distances for a particle crossing a drift cell and in it is shown how the shorter drift times are going to be most affected by the non-linearity of the field electric field. This is shown in Fig. 4.3 as the wire signal wire position, W_{min}, and requires a LUT offset.

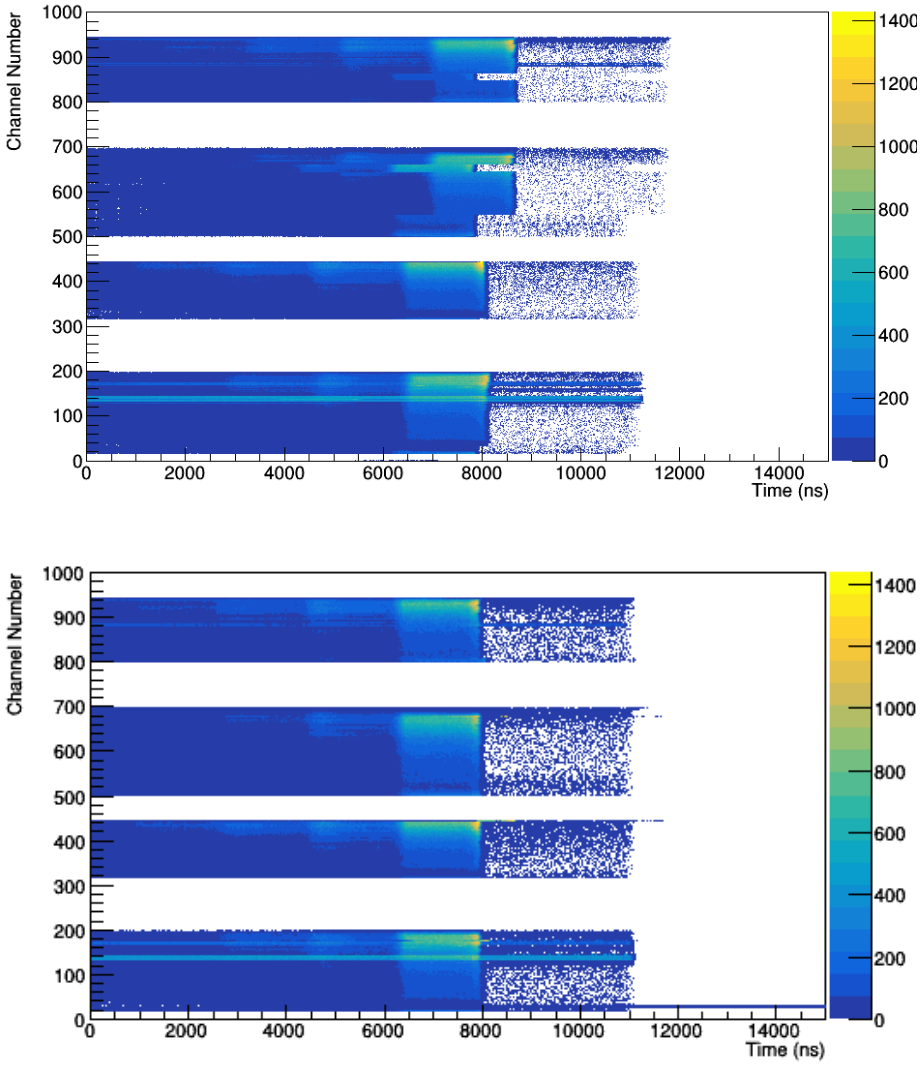

Figure 4.2: Top: A drift time spectrum that has not been corrected shows the time difference between the different TDC modules. Bottom: A drift time spectrum that has been corrected shows that the time difference between the different TDC modules have been remedied.

In order to visualise the effects of this aberration and quantify the offset required, a 2-D resolution spectrum for each wireplane is made. It is generated by plotting the relative distance where the particle crosses the wire plane against the slope difference shown in Fig. 4.3:

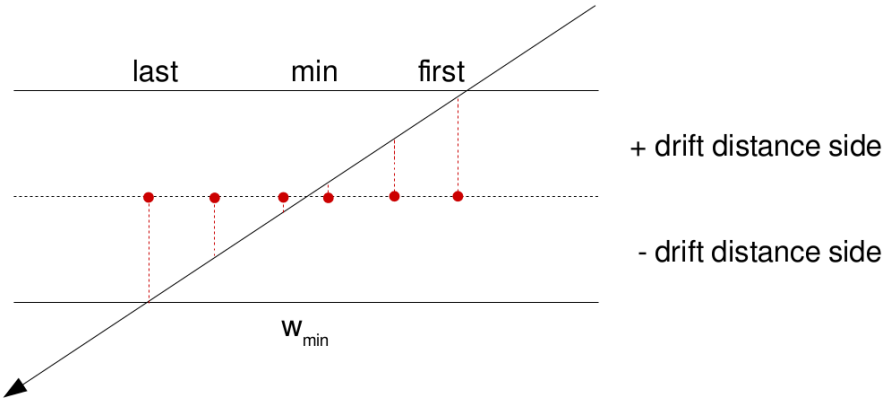

Figure 4.3: A schematic representation of how a charged particle is characterised in the drift cells. The positive and negative drift distances indicate which direction the ionised molecules drift in the drift cell and W_{min} is the center of the drift cell through which the particle crosses.

$$SlopeDif = \frac{d_{first} - d_{min}}{w_{first} - w_{min}} + \frac{d_{first} - d_{min}}{w_{first} - w_{min}}, \tag{4.4}$$

where d and w represent the drift time and drift cell position with the subscripts being shown in Fig. 4.3.
Fig. 4.4 clearly shows a misalignment of the central band on the left panel which indicates that the drift times are not being converted into drift distances correctly for the U2 VDC. This is corrected by introducing a LUT offset after which the central band becomes continuous as seen in Fig. 4.5. Table 4.3 shows the values of the LUT that were required to produce good drift times.

Table 4.1: Table of the LUT offsets used for this data.

Wireplane	Offset (100ps)
X1	0
X2	-3
U1	-3
U2	5

Fig. 4.6 shows the effect of the LUT offsets on the focal plane position spectrum. The shorter drift times undergo a significant change to drift position whereas the longer drift times are changed less.

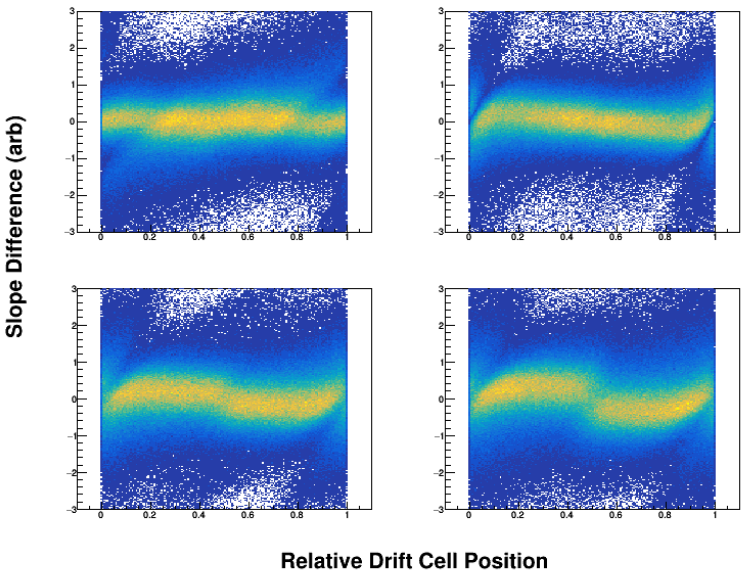

Figure 4.4: Resolution plots showing the slope difference defined in Eqn. 4.4 versus the relative drift cell position. Top: The X2 2-D resolution plot on the right indicates that the LUT is in need of minor negative shift whereas the X1 plot is properly centered. Bottom: The U2 2-D resolution plot on the right indicates that the LUT is in need of minor positive shift whereas the U1 plot only requires a small negative adjustment.

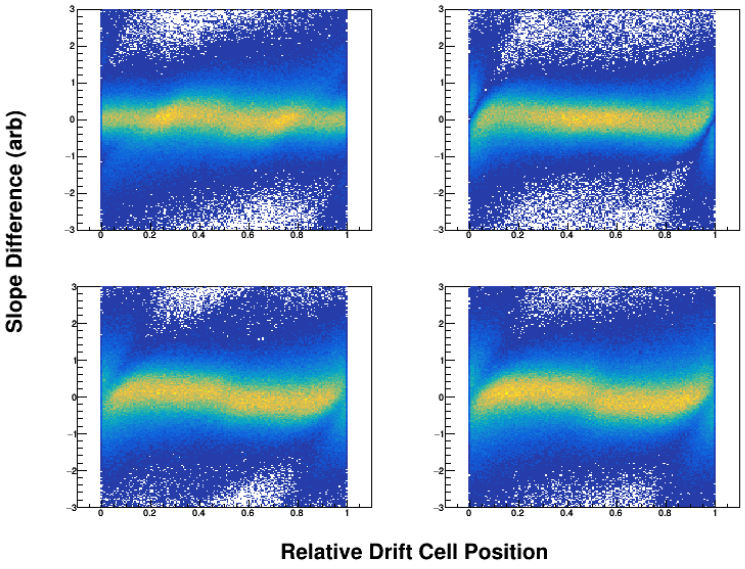

Figure 4.5: Resolution plots showing the slope difference defined in Eqn. 4.4 versus the relative drift cell position. Top: The X wire-plane 2-D resolution plot post corrections. Bottom: The U wire-plane 2-D resolution plot post corrections.

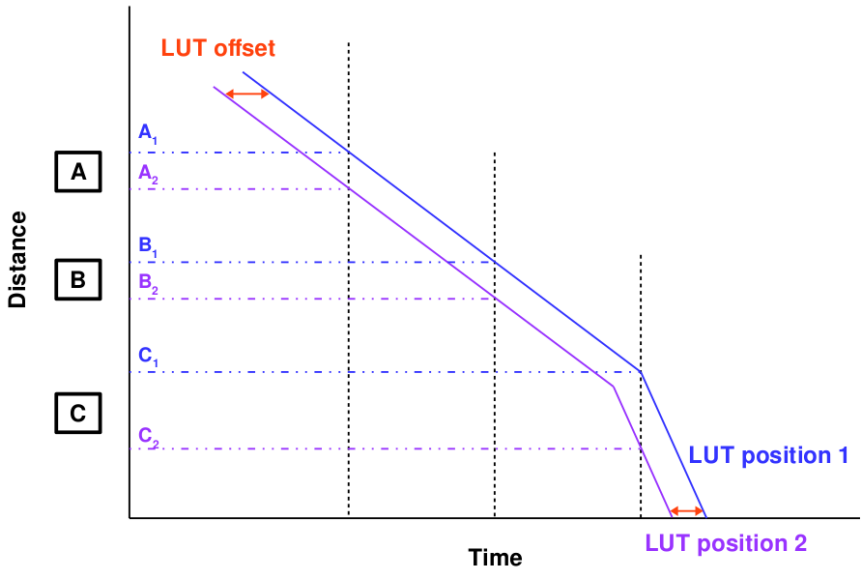

Figure 4.6: Figure showing the effect of the LUT offsets.

4.1.4 Angle Calibrations

The K600 was setup in high dispersion mode at 6.9° and at 4.2% underfocus mode for the collimator runs. The horizontal angle calibration is used to apply the lineshape corrections in Section 4.3.3.
The angle calibration for this experiment was done using a multi-hole collimator, affectionately known as a pepperpot, to extract scattering angles from focal plane angles. By passing the elastic peaks through the pepperpot, a series of Gaussian peaks appear at the focal plane each coinciding with a hole on the pepperpot. The parameters of the Gaussian peaks provide the spatial coordinates required to determine a conversion equation between focal plane angle (θ_{fp}) from the detector to the scattering angle of the projectile at the target (θ_{scat}). This conversion equation uses the spatial coordinates of the focal plan as input and the known scattering angles of the collimator to fix the constants of the first order conversion polynomial:

$$\theta_{scat} = (a_1 x_{fp} + a_0)\theta_{fp} + b_1 x_{fp} + b_0. \tag{4.5}$$

The focal plane angle of the holes were determined by fitting a Gaussian to Fig. 4.8. From Eqn. 4.5 parameters a_1 and a_0 are found from the slope of the θ_{SCAT} and x_{fp} graphs and are shown in the top panel of Fig. 4.9. The b_1 and b_0 parameters are found by plotting the offsets as a function of focal plane position. The focal plane angles plotted against the scattering angles of the pepperpot runs are shown in Fig. 4.9.

Figure 4.7: Photo of the pepperpot collimator used during experiments. The holes each span 0.41^0 and the centroids are 0.81^0 degrees apart.

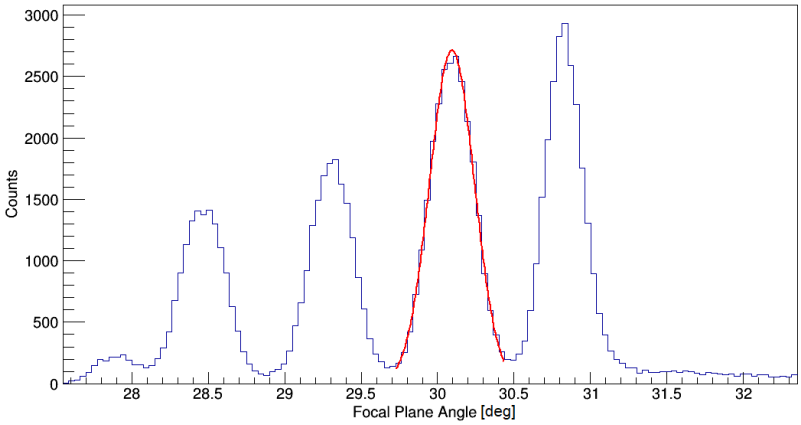

Figure 4.8: Figure showing the focal plane angle obtained from the pepperpot run and an example of the Gaussian fit used to obtain the centroid of each hole.

Table 4.2: θ_{fp} to θ_{scat} conversion coefficients

Conversion coefficient	Value of coefficients.
a_1	$-1.686 \cdot 10^{-6}$
a_0	0.02809
b_1	30.01
b_0	30.01

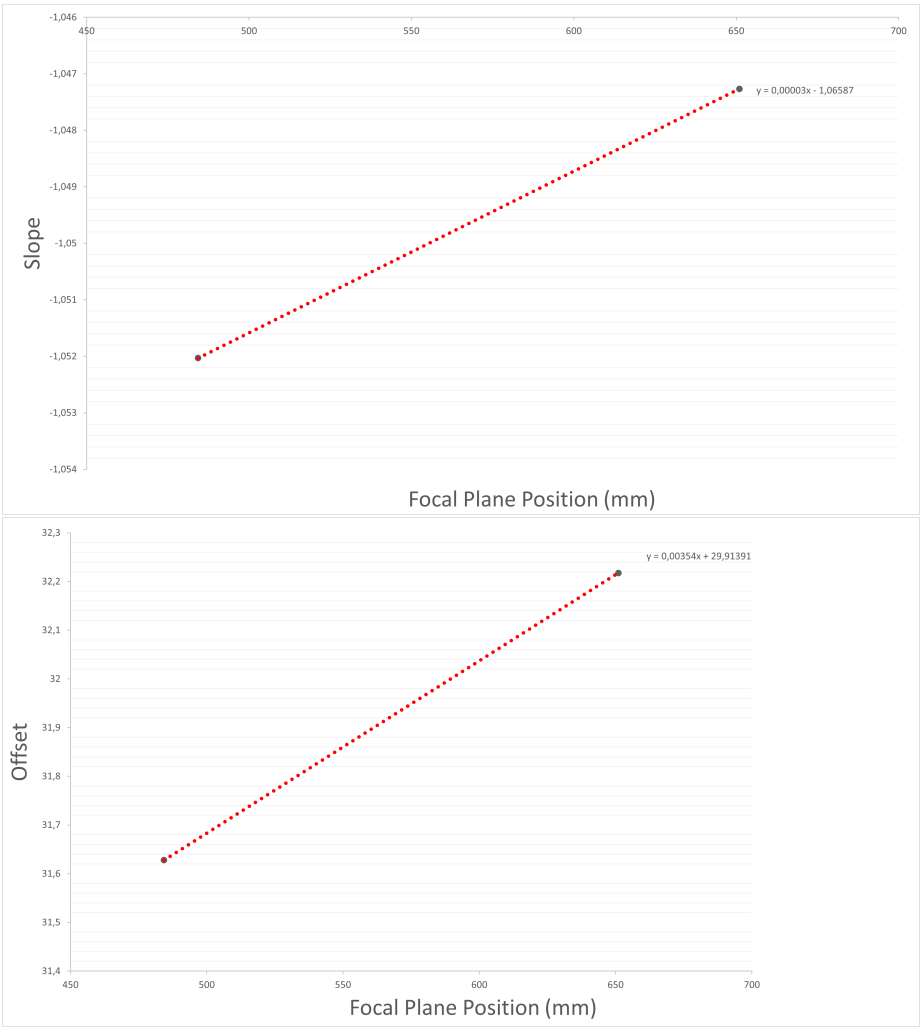

Figure 4.9: Top: The scattering coefficients a_0 and a_1 are calculated using the slope and offset of this graph. Bottom: The scattering coefficients b_0 and b_1 are calculated using the slope and offset of this graph.

Note that during the angle calibration runs the beam was unstable and as such only 2 of the planned 5 runs were usable. However, the results of the calibration were compared and found to be in good agreement with previously obtained results from similar calibrations.

4.1.5 Position Offsets

This experiment was run over the course of two weekends and there are small differences in focal plane positions. These position shifts are caused by the conditions of the accelerated beam at the source and the SSC. This presents a problem when trying to combine multiple sets of data and reduces the resolution of the energies considerably. It is fixed by applying offsets to each of the individual runs using a set of calibrated peak energies. In this case, the 10.711 MeV peak in ^{24}Mg was used to align all of the runs. The 2mm difference in the FWHM is clearly visible in Fig. 4.10.

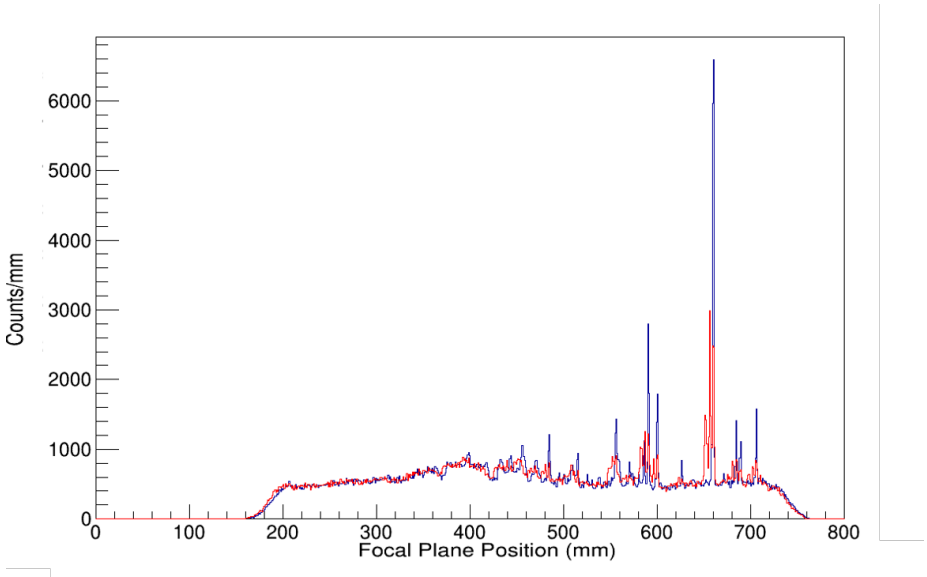

Figure 4.10: The combined position spectrum of ^{24}Mg showing the difference in the position spectrum before (red) and after (blue) offsets were introduced.

4.1.6 Lineshape Corrections

Lineshape corrections are part of the procedure used to increase the resolving power of the spectrometer beyond the capabilities of the K- and H-coils. This procedure helps correct some of the angular deviations that the kinematic correction process could not eliminate. In order to apply a lineshape correction a well resolved and strong state is required. The slant of this curve can be used

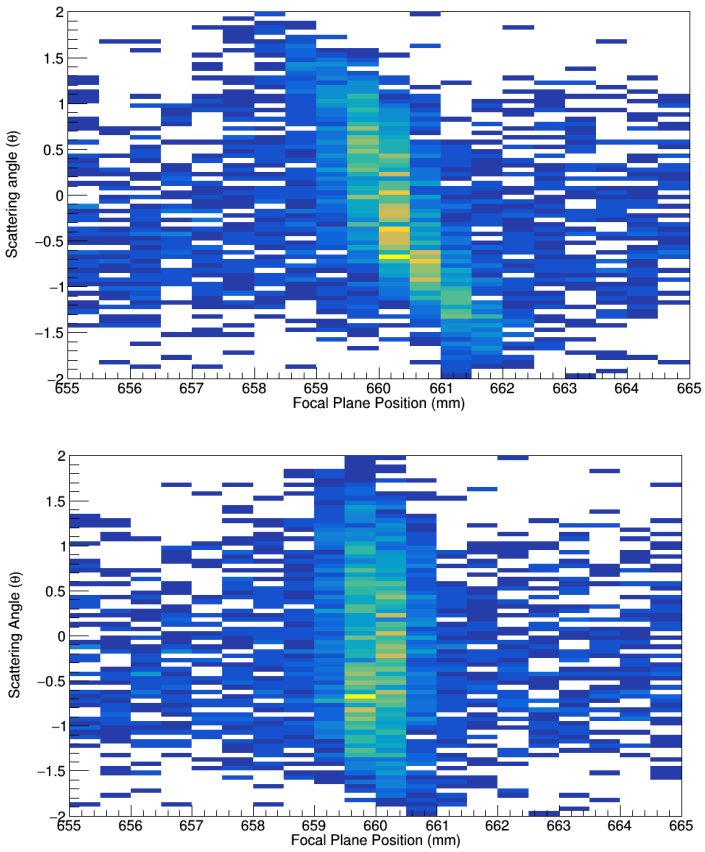

Figure 4.11: Figure showing a the 10.711 MeV state in ^{24}Mg before lineshape correction (top) and after lineshape correction (bottom).

to extract a polynomial fit to correct it. The points are taken from projections to the x-axis that are then fitted with a gaussian to determine their location. After generating a fit, it was determined that a fifth degree polynomial of the following form was best suited:

$$X_C = A_0 + A_1\theta_{SCAT} + A_2\theta^2_{SCAT} + A_3\theta^3_{SCAT} + A_4\theta^4_{SCAT} + A_5\theta^5_{SCAT} \quad (4.6)$$

The FWHM of the states improved from $\approx$ 40 keV before correction to $\approx$ 30 keV after the lineshape correction. These effects are evident in Fig.4.13.

Table 4.3: List of lineshape correction coefficients.

Coefficient order	Value
A0	660.034
A1	0.1769
A2	-0.2429
A3	0.4765
A4	0.0626
A5	-0.05547

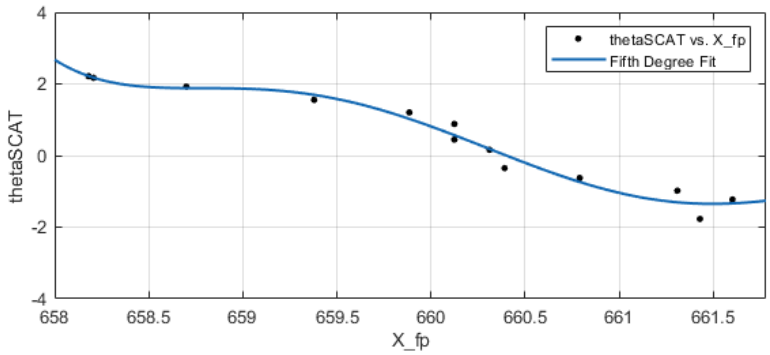

Figure 4.12: The fifth order polynomial (blue line) generated by fitting the unaligned 10.711 MeV state of ^{24}Mg at 660 mm.

4.2 Preparation of data

4.2.1 Background subtraction

When the K600 is operated in focused mode, the majority of signal events occur around the vertical middle of the focal plane detectors. To ensure that the background is correctly estimated it is imperative to check the shape of the background in both the X and the Y planes. To do this, a region in both the X and the Y focal planes that is devoid of any strong states is required. Ideally, two such strips are required for both cases to verify the consistency of the background.
The shape of the background is obtained by fitting and comparing the regions above and below the vertical extent of the excited states as well as to the left and right of a well resolved state as seen in Fig. 4.14. This is done to ensure that the regions from which the background function is generated is consistent throughout the focal plane. The Y1 background is shown in the top panel of Fig.4.15 and corresponds to the yellow region in Fig. 4.14 , where it can be seen that the background has a constant shape throughout the vertical spectrum. The X1 spectrum gradually decreases along the focal plane towards higher excitation energies and is shown as the red region in Fig. 4.14. After a

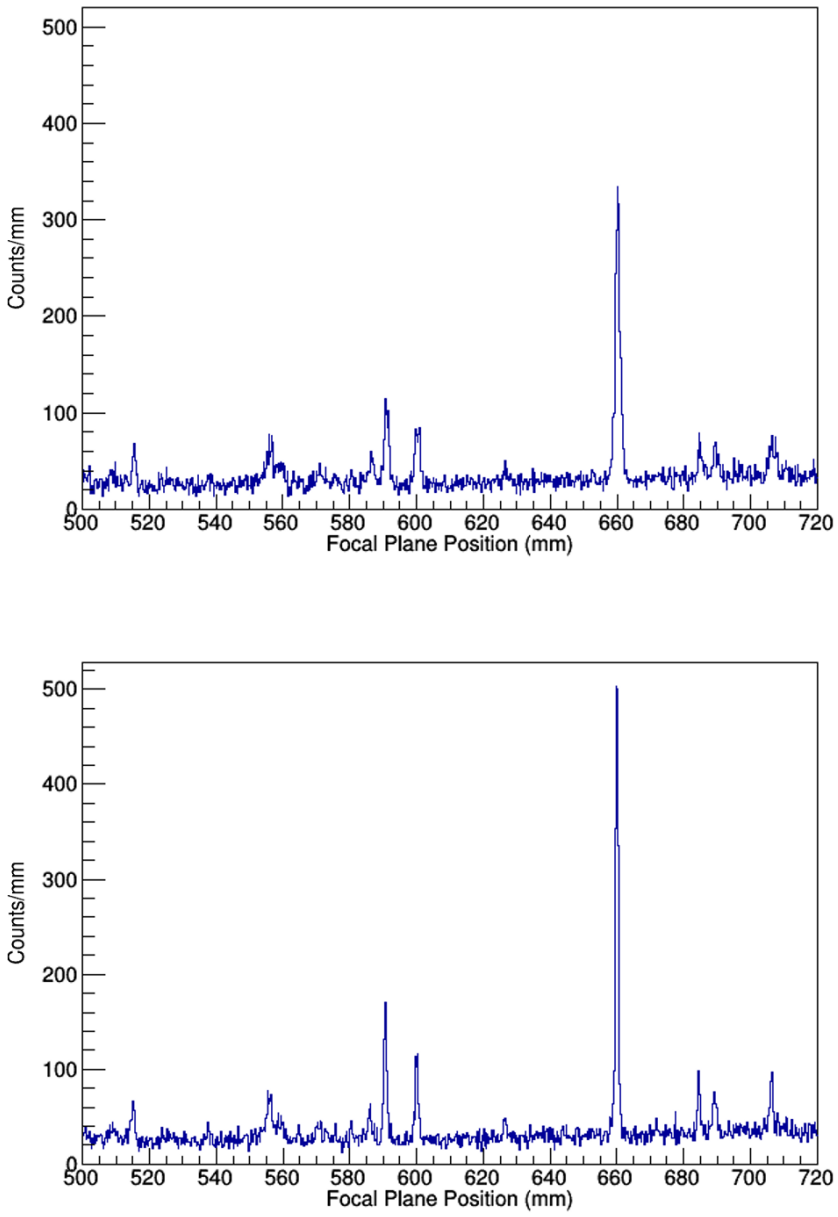

Figure 4.13: The net effect of the lineshape corrections are seen in the increase of the peak resolutions from the top panel to the bottom panel.

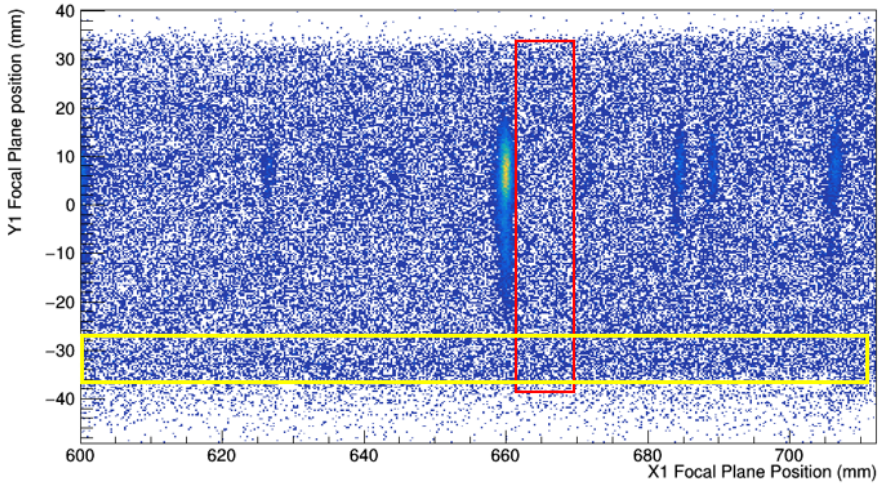

Figure 4.14: Enhanced image showing the regions of interest for the background subtraction. The vertical width of the state is 40 mm between -20 and 20. Hence the background regions of interest is between -25 and -35. Likewise for the focal plane position the background region is between 665 and 675.

polynomial fit for the background in each region is obtained, it is then normalised to the signal region. The normalisation factor is given by:

$$Norm = \frac{Width_{Signal}}{Width_{Background}}. \tag{4.7}$$

The signal region is 40 mm wide and the background 10 mm, thus a normalisation factor of 4 is applied to the background spectrum. The scaled up background function is then subtracted from the X1 position spectrum.
The focal plane position spectrum before and after background subtraction is shown in Fig.4.16.

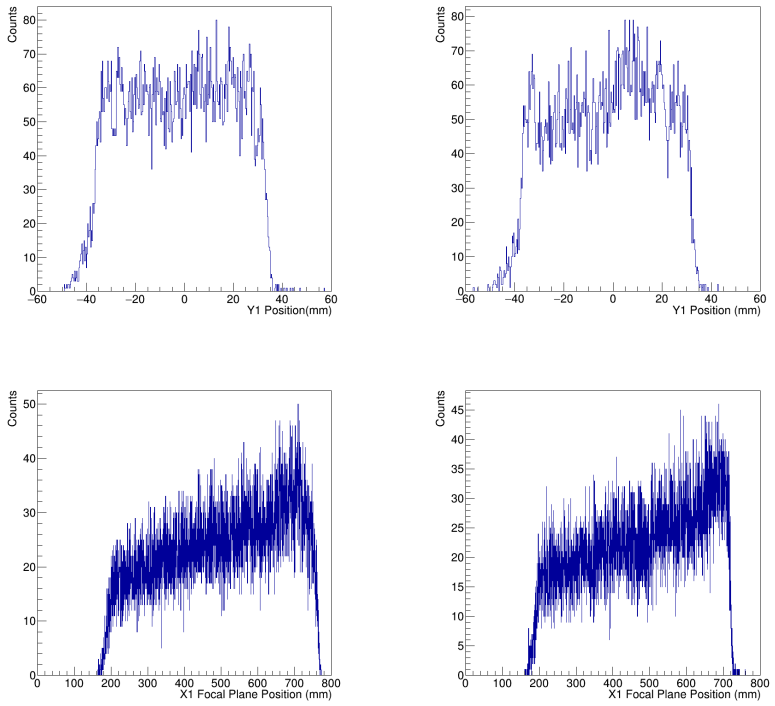

Figure 4.15: Top: Y1 Focal plane position spectrum showing the vertical background shape corresponding to the red gate in Fig. 4.14 to the right of the 10.711 MeV state at 660 mm in the left panel and the background to the left of the 10.711 MeV state is shown in the right panel. Bottom: X1 Focal plane position spectrum showing the horizontal background shape corresponding to the yellow gate in Fig. 4.14 below the 10.711 MeV state at 660mm in the left panel and above the 10.711 MeV state in the right panel.

4.2.2 Energy Calibration

The conversion from focal plane position to energy is done by fitting the known peaks in ^{24}Mg to the position spectrum obtained at the focal plane. The states used were the states at 9.305, 10.711 and 12.954 MeV which were situated at 706.15, 659.98 and 590.62 mm. The conversion polynomial is given by:

$$Energy = c_2 \cdot x_1^2 + c_1 \cdot x_1 + c_0, \tag{4.8}$$

and the respective values of the coefficients are given in Table: 4.4.
The energy calibration leads to energies that are well within 1% of their known values as seen in Table: 4.5. The state at 11.73 MeV has the largest FWHM at 36.8 keV and this is due to it the being the weakest excitation of all the states

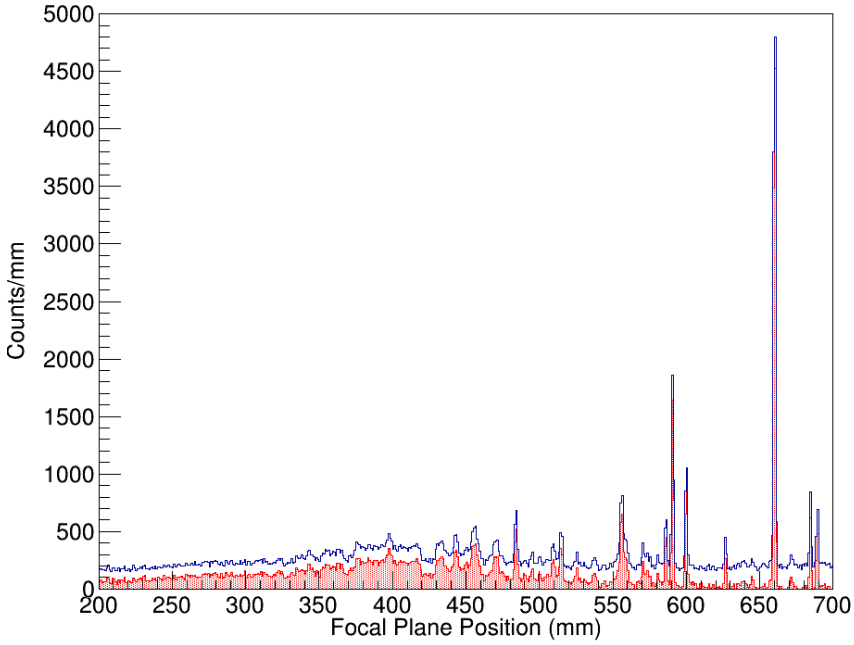

Figure 4.16: The background unsubtracted (blue) and background subtracted spectra (red).

Table 4.4: Focal plane to energy conversion coefficients

Conversion coefficient	Value of coefficient
c_2	$-1.686 \cdot 10^{-6}$
c_1	0.02809
c_0	30.01

being compared. There is a clustering of states in the vicinity of the 13.851 MeV state which leads to it having the second largest FWHM.

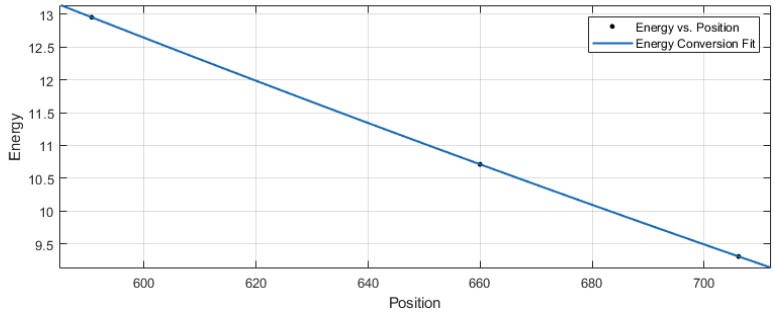

Figure 4.17: Plot showing the quadratic energy fit to focal plane position of the 9.305, 10.711 and 12.954 MeV states.

Table 4.5: Peak energies and uncertainties compared to their known values [62].

ENSDF (MeV)	iThemba (MeV)	FWHM (keV)	Parity
9.305	9.3133 (5)	30.0	+0
9.828	9.836 (7)	32.4	+1
9.967	9.97 (7)	24.2	+1
10.711	10.7 (1)	28.1	+1
11.728	11.7 (1)	36.8	+0
12.526	12.53 (3)	34.1	+1 +2
12.8159	12.816 (2)	30.2	+1 +2
12.954	12.953 (4)	36.3	+1 +2
13.88	13.851 (7)	30.1	Unknown

4.2.3 Cross section calculation

The extraction of the experimental double-differential cross section is the culmination of all the experimental details described thus far. It is the physical quantity that is used to describe the nuclear reaction and structure of the target as a function of energy and solid angle. The double-differential cross section is used to calculate the photoabsorption cross section which is the physical quantity being investigated in this thesis. The experimental double-differential cross section, in the context of the K600 setup, is calculated using the following formula:

$$\frac{d^2\sigma}{d\Omega dE} = \frac{10^{27} \cdot N_c}{N_0 \cdot \rho \cdot D \cdot \Delta\Omega \cdot \Delta E \cdot \epsilon_{tot}} \tag{4.9}$$

where:

- N_0 is the number of protons incident on the target.

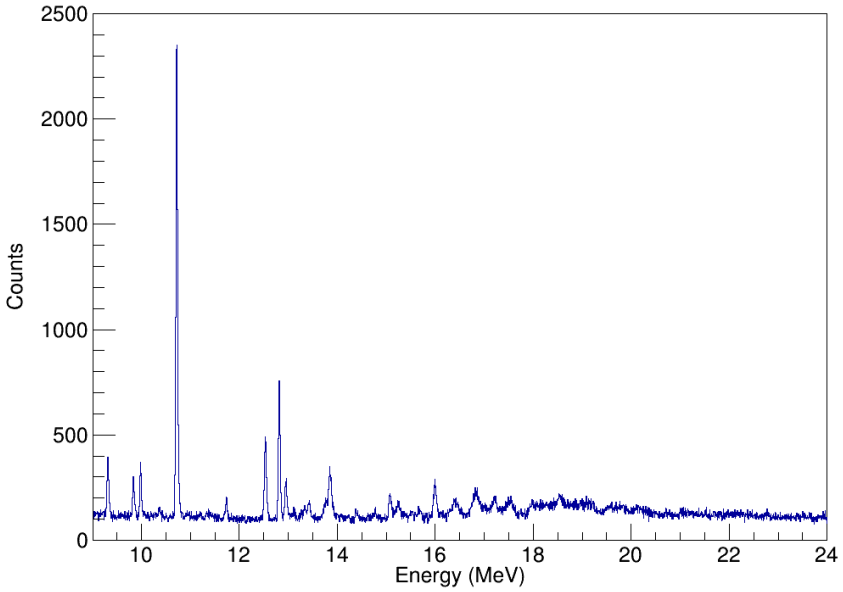

Figure 4.18: The count spectrum after being converted from focal plane position to excitation energy.

- N_c is the number of counts in a bin.
- ρ is the areal density of the target nucleus (2.1 mg/cm^2).
- $\Delta\Omega$ is the solid angle of the detector used in the K600 and has a value of 3.41 msr.
- ΔE is the energy bin of the histogram (10 keV for Fig. 4.19).
- ϵ_{tot} is the efficiency of the VDC's used in the K600.
- D is the fraction of events that the electronics resolved.

The number of incident protons are calculated using a current integrator system:

$$N_0 = \frac{CI \cdot R \cdot 10^{-12}}{e}, \tag{4.10}$$

where $CI \cdot R$ is the current integrator readout times its range setting (in nA) and e is the fundamental unit of charge. This represents a count rate of 1000 pulses per each nA of current impinging on the target. The efficiency of each wire-plane is calculated in the following way:

$$\epsilon(X_{1,2}) = \frac{N_{events}(X_1X_2, U_1, U_2)}{N_{events}(X_{1,2}, U_1, U_2)}, \tag{4.11}$$

where $N_{events}(X_1X_2, U_1, U_2)$ is the number of events that pass the criteria for good events in the X_1, X_2, U_1 and U_2 chambers. The criteria for a good event is as follows:

- Number of wires hit is between 3 and 6.
- Time of flight and the plastic scintillators signals are in well resolved regions.

The ranges of individual efficiency were between 80% and 85% for each of the wire planes. The total efficiency is given by:

$$\epsilon_{tot} = \epsilon_{X1} \cdot \epsilon_{X2} \cdot \epsilon_{U1} \cdot \epsilon_{U2}, \tag{4.12}$$

which leads to a ϵ_{tot} of 55%. The fraction of events that were resolved is given by the resolving time, D:

$$D = \frac{S_{IH}}{S_{UH}}, \tag{4.13}$$

where S_{IH} is the readout of the inhibited counter and S_{UH} is the uninhibited counter readout as defined in Section 3.2.2.

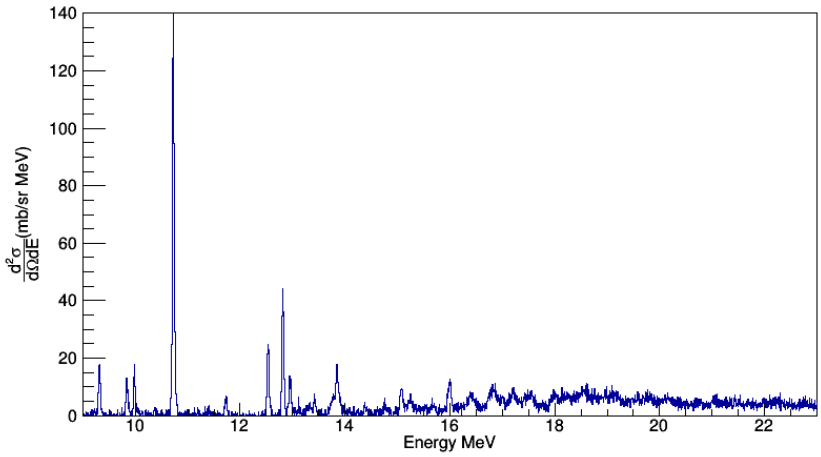

Figure 4.19: Spectrum showing the Double Differential Cross Section obtained from the excitation energy spectrum.

The double differential cross section spectrum is given in Fig. 4.19. It shows well resolved peaks and a successful implementation of the background reduction procedure. The associated statistical errors for each bin were calculated using:

$$\Delta \frac{d^2\sigma}{d\Omega dE} = \frac{1}{\sqrt{N_c}} \frac{d^2\sigma}{d\Omega d\sigma}. \tag{4.14}$$

The full contributions of the sources of error in each of the procedures is given in Table 4.6. The most significant source of errors were the target density and systematic errors. The energy loss in the target is a negligible contribution when doing experiments at large proton beam energies on light nuclei.

Table 4.6: Sources of error in the cross section calculation.

Source of Error	Error Percentage
Target Density Uncertainty	6%
Detector dead time	3%
Energy loss in target	<0.1%
Systematic Error	4% - 6%
Energy Calibration	1%

Chapter 5

Results and Discussion

This chapter focuses on the conversion of the (p,p') energy spectrum into a spectrum of equivalent absorbed photons with the aim of comparing this method to previous studies.

Overview of the experimentally obtained inelastic scattering data

The experimental double differential cross section that was obtained using Eqn. 2.13 after following the procedures highlighted in previous chapters is shown in Fig. 4.19. The focal plane detector is tilted near the edges which cause events at the edges of the spectrum to not be accepted and limits the practical energy range of the focal plane to between 9 MeV and 23 MeV. This can be seen in the range of the double differential cross section spectrum shown in Fig. 4.19, which is the spectrum that is converted to spectrum of equivalent absorbed photons in the following section.

It is important to note that GRs other than the IVGDR are still present in this spectrum. In order to properly subtract the contributions from these GRs, a DWBA (Distorted-Wave Born Approximation) [63] calculation is required to estimate the relative strength of each of these multipoles and subtract their contributions from the double differential cross section. In the case of this dissertation, a DWBA was not possible as the process of calculating the relevant microscopic form factors for inelastic proton scattering on ^{24}Mg at 200 MeV is being calculated by a nuclear structure theorist in the research group. Without the DWBA calculation it is erroneous to subtract the contributions of these contributions but a rough estimate of their relative strength can be obtained from similar experiments. In the case of inelastic proton scattering elements such as ^{142}Nd, ^{56}Fe, ^{40}Ca and ^{27}Al, the contributions of the ISGQR and ISGMR in the IVGDR region were less than 10%. Once the microscopic form factors have been obtained, the ISGMR and ISGQR can be eliminated from this spectrum and the results will improve. An example of a DWBA calculation of ^{142}Nd for 200 MeV inelastic proton scattering is shown in Fig.5.1. In it, the relative

strength of the ISGQR and IVGDR is compared at 15 MeV excitation energy. By using the DWBA comparison and the known location and widths for the GRs, the other GRs can be accounted for and subtracted from the double differential cross section as shown in Fig. 5.2. The phenomenological background component at higher energies is discussed in Section 5.2.2.

5.1 Virtual photon production

To ensure that the spectrum is purely due to the electromagnetic interaction, it is possible to calculate the maximum scattering angle at which strong force interactions starts appearing by use of a relativistic Rutherford scattering equation [65]:

$$\theta_{lab}^{max} = \frac{Z_{eff}}{b\mu\gamma\beta^2}, \tag{5.1}$$

where Z_{eff} is the product of projectile and target charge multiplied by the fundamental charge squared e^2, b is the impact parameter, μ is the reduced mass, γ is Lorentz boost and β^2 is the velocity in natural units [64]. The maximum scattering angle at which nuclear interactions start appearing given these conditions is at 1.89°. The nuclear contribution is thus negligible to interaction spectrum, which has an angular range of 0° to 2°.

The production of virtual photons for ^{24}Mg(p,p')^{24}Mg inelastic scattering was calculated using the procedure highlighted in Chapters 3 and 4. The Eikonal model for calculating virtual photon production is necessary as the experiment takes place at very small scattering angles and the elimination of the pole at zero degrees is vital. The model also produces more realistic results by including diffuseness and retardation effects as discussed in Section 2.2. The number of virtual photons produced were calculated at discrete energy steps of 10 keV in the energy ranges between 9 MeV and 23 MeV. The angles for virtual photon production are also smoothly varied over the angular opening of the aperture of the detector from 0° to 2° in steps of 0.15°. As can be seen in Fig. 2.9, the amount of virtual photons of E1 polarity produced gradually decreases as the energy of the interaction increases, owning to higher momentum transfer reactions being favored at higher energies. The number of E1-photons produced also decreases as scattering angle of the projectile increases owning to the E1 reaction channel being at its strongest at 0°. Due to the excitation spectrum being given as the average over the scattering angles, the average of the virtual photon production across the whole experimental angular range is used to calculate the photoabsorption cross section and is shown in the bottom panel of Fig. 5.3.

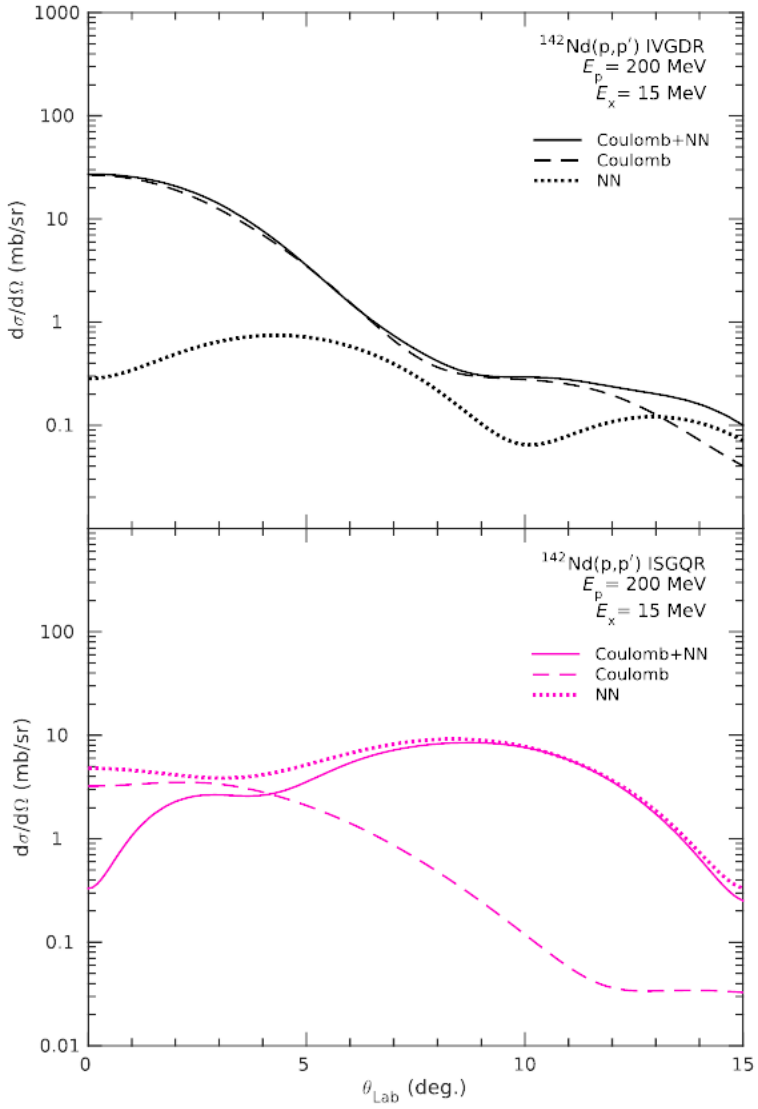

Figure 5.1: A DWBA calculation on ^{142}Nd showing the contribution of the Coulomb and nuclear interactions combined and separated. The IVGDR at 0° is shown to have a cross section an order of magnitude larger than that of the ISGQR [48].

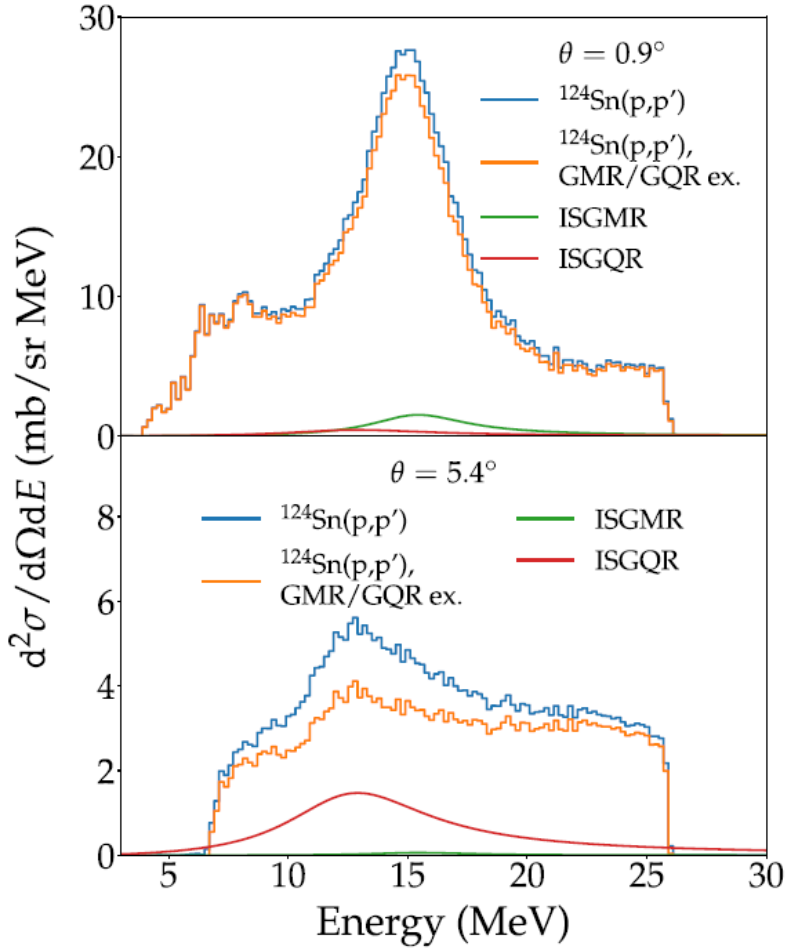

Figure 5.2: The double differential cross section for ^{124}Sn(p,p') at 200 MeV. The contributions of the ISGMR (green) and the ISGQR (Red) present are shown for different angular distributions. The spectra shown are before (blue) and after (orange) subtraction of the ISGMR and ISGQR.[64]

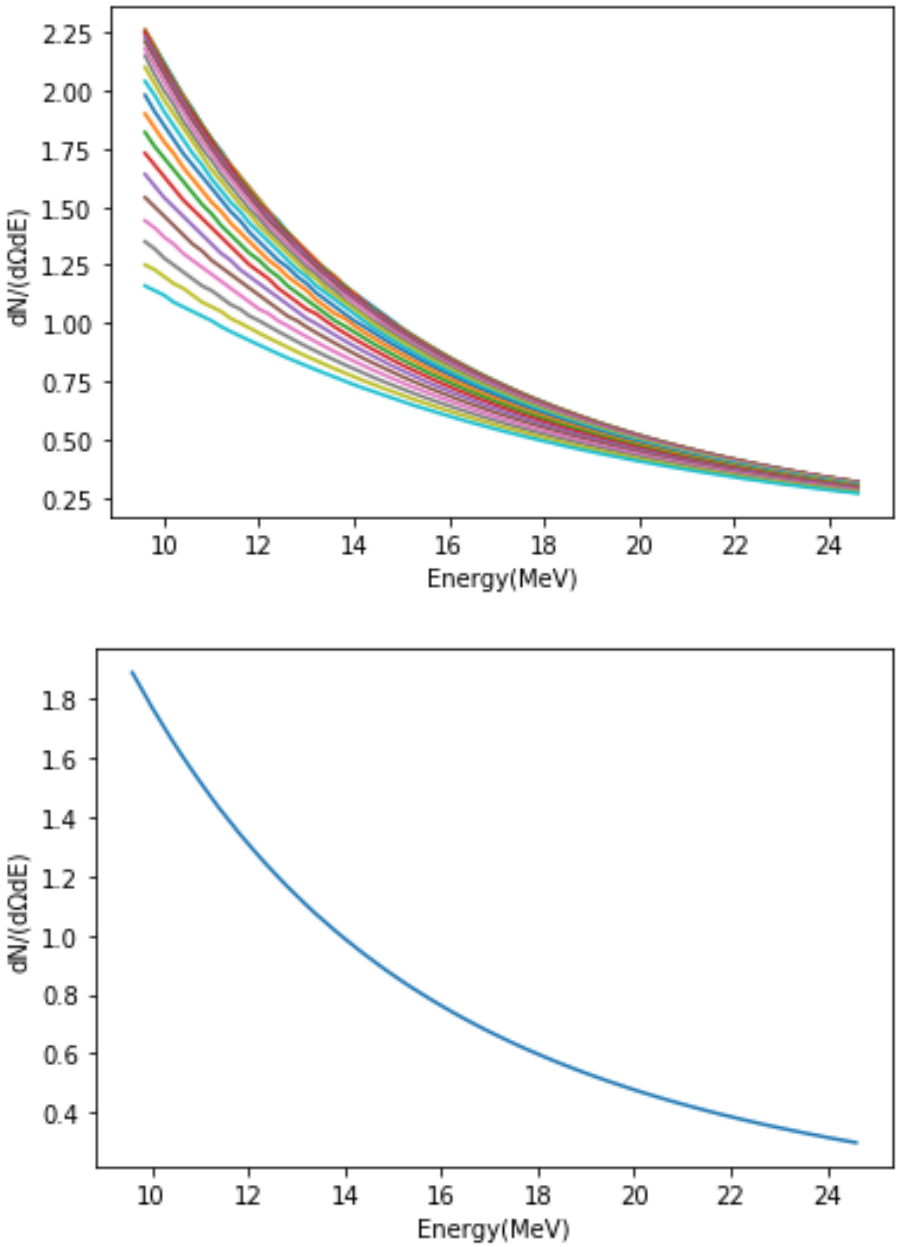

Figure 5.3: Top: Calculated number of virtual photons produced in the angular range between 0° and 2° for 200 MeV protons impinging on ^{24}Mg. The lowest teal line represents the 2° virtual photon production and each line above it is the virtual photon production at 0.15° less. Bottom: The average amount of virtual photons produced between 0° and 2° for 200 MeV protons impinging on ^{24}Mg.

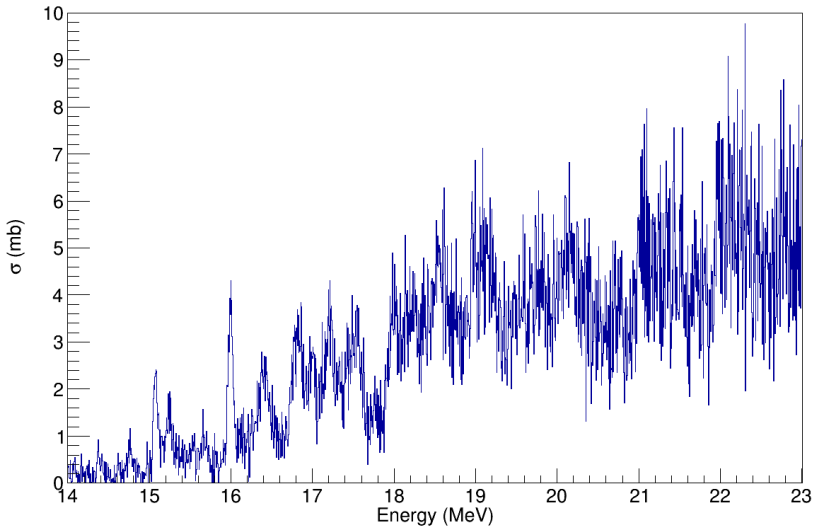

Figure 5.4: The E1 photoabsorption cross section versus excitation energy spectrum. The IVGDR becomes visible in this spectrum as an increase in strength between 14 and 23 MeV.

5.2 Photoabsorption Spectrum

To obtain the photoabsorption cross section from the double differential cross section, the following equation from Chapter 3 is used:

$$\frac{d^2\sigma}{d\Omega dE_\gamma} = f_{nor}\frac{1}{E_\gamma}\frac{dN_{E1}\sigma_\gamma^{\pi\lambda}}{d\Omega}(E_\gamma). \tag{5.2}$$

The applicable version of this equation is:

$$\sigma_\gamma^{\pi\lambda}(E_\gamma) = f_{nor}\frac{d^2\sigma}{d\Omega dE_\gamma}\left(\frac{dN_{E1}}{d\Omega}(E_\gamma)\right)^{-1}E_\gamma. \tag{5.3}$$

The inclusion of a normalisation factor, f_{nor}, being a notable difference. This normalisation factor is an experimental detail that has been found in similar experiments at iThemba LABS [48]. Although it is yet unknown what exactly leads to the need for this normalisation factor, there is some evidence that suggests it is related to the vertical angular acceptance of the K600 spectrometer. In the case of neodymium isotopes the normalisation factor was 0.42 for ^{144,146,148,150}Nd and 0.6 for ^{140}Nd [66] whereas in a collection of lighter isotopes such as ^{58}Ni, ^{56}Fe, ^{40}Ca and ^{27}Al the normalisation factor was found to be roughly 0.6 [51] and in agreement with this experiment on ^{24}Mg.

5.2.1 Comparison to previous data sets

The data set used for comparison during this analysis was obtained in 1966 by Dolbilkin et al [67] using the Lebedev Physical Institute synchrotron at 260 MeV. The measurements were performed in steps of 40 keV but were then averaged to bins of 200 keV. In order to make useful comparisons between the data obtained by this method and this experiment, the data from the current experiment had to be renormalised to 200 keV steps. The calculations were performed using the finer bins and then rebinned at the end of the calculations as this preserved some of the finer structure present in the spectrum. Figs. 5.4 and 5.5 show the difference before and after rebinning. The (p,p') spectrum contains single particle states of unknown parity that cause deviations from the systematic data. The three peaks between 17 MeV and 18 MeV are examples of these unknown parity states is the continuum. The fine structure of the IVGDR can be investigated and the parity of these peaks has been quantified in other experiments using high resolution techniques [68].

After this normalisation and the rebinning has been applied to the photoabsorption spectrum the agreement between the (γ, abs) and (p, p') data is clear. In the fine structure of Fig. 5.5 the neutron escape threshold in both the full gamma absorption (γ, abs) and (p,p') spectra at 16 MeV is clearly present. This is shown as the distinct absence of data in the (γ, abs) in the region highlighted by Fig5.6 as the (γ, abs) setup used in that experiment was not sensitive to neutron emission. The k_0 section (as described in Section: 2.1) of the IVGDR is in agreement with both the previous experiment and the systematics taken from the nuclear Reference Input Parameter Library (RIPL)[38]. Some discrepancies are seen as well, most notably the two broad states at just above 15 MeV and at 16.5 MeV and the considerable excess of strength beyond 21 MeV.

There is an excess of strength in the region beyond the k_0 peak in the IVGDR of ^{24}Mg from 21 MeV upwards. This excess is caused by mainly two reasons. The first reason is the presence of the ISGQR, and to a lesser extent the ISGMR, that has not been subtracted from the (p, p') cross section spectrum. In order to properly address this excess, a DWBA calculation is required to estimate the relative strengths of these contributions and subtract the corresponding backgrounds for each multipolarity. The conversion from double differential cross section to photoabsorption cross section is highly sensitive to background in the higher energy regions due to shape of the virtual photon production spectrum it is divided by to obtain the photoabsorption cross section. A difference of 2% at 20 MeV in the double differential cross section will lead to a 10% difference in the photoabsorbtion cross section. An example of a DWBA calculation of ^{142}Nd for 200 MeV inelastic proton scattering is shown in Fig. 5.1. In it the relative strength of the ISGQR and IVGDR is compared for 15 MeV excitation energy. By using the DWBA comparison and the known location and widths for the GRs, the other GRs can be accounted for and subtracted from the double differential cross section.

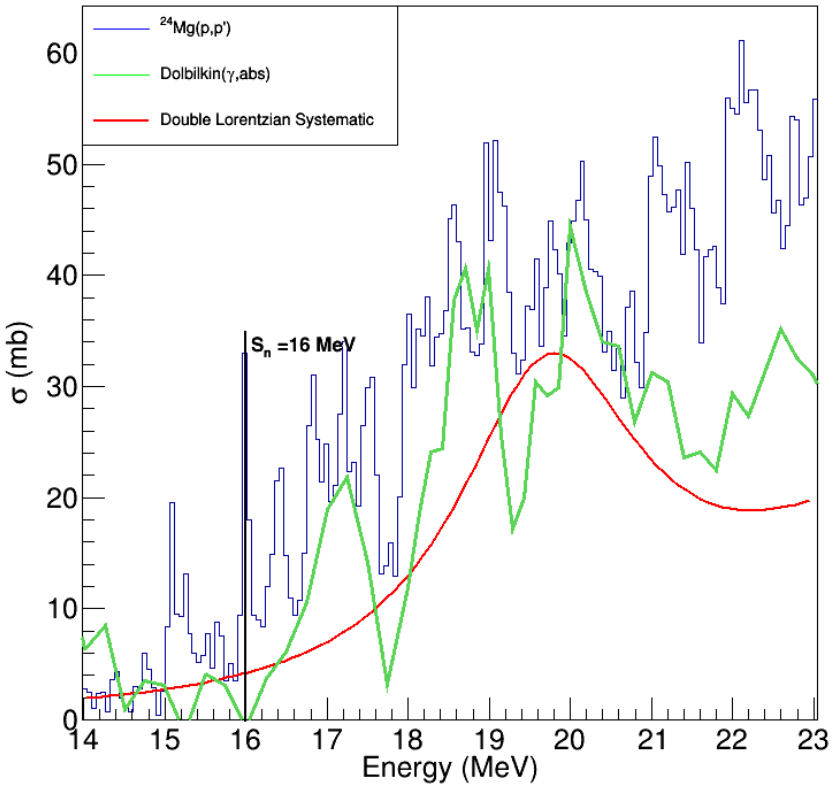

Figure 5.5: The E1 photoabsorption cross section the after it has been rebinned and normalised. The data from this experiment is shown compared to a previous (γ, abs) data set and the systematic double Lorenzian predicted by theory.

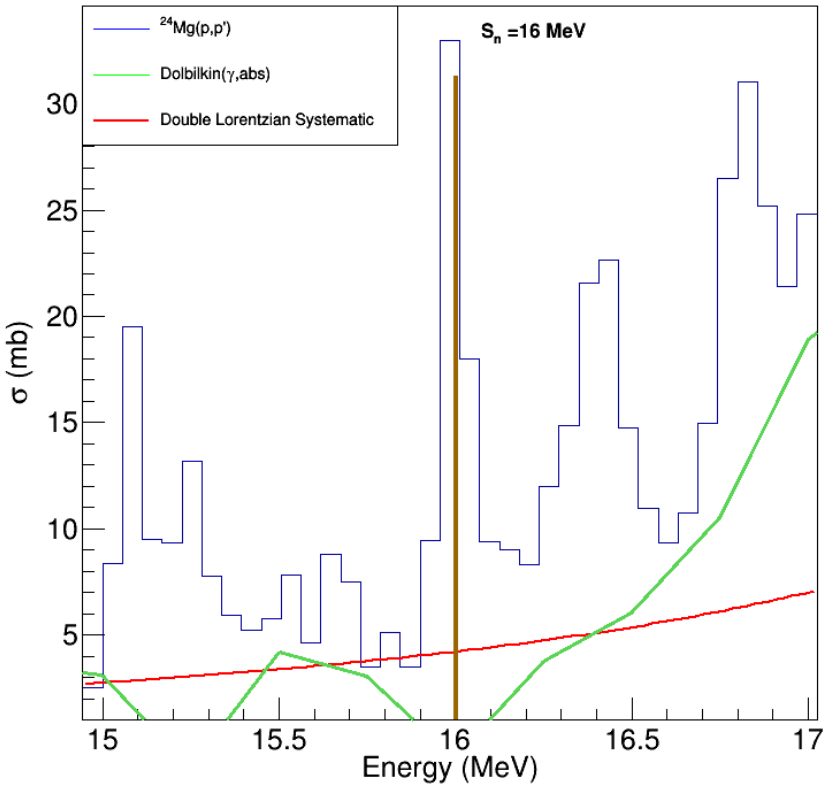

Figure 5.6: The section of the spectrum highlighting the significant difference between the previous (γ, abs) [67] experiment and the (p,p') spectrum near the neutron threshold.

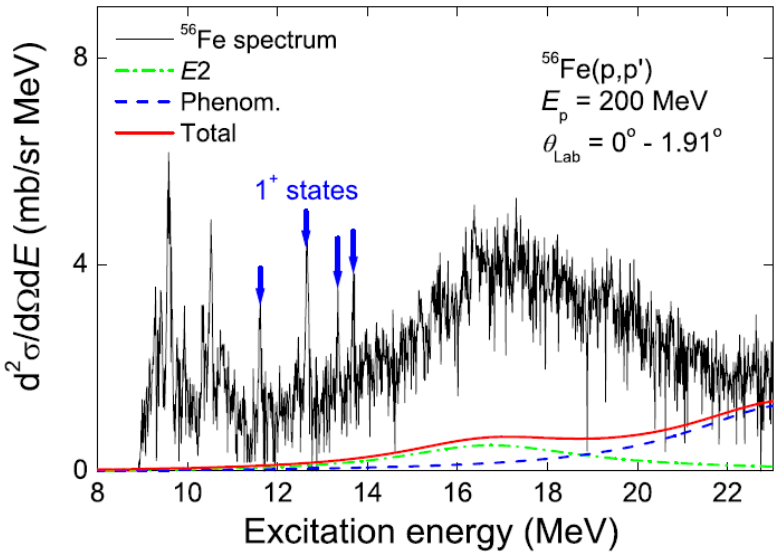

Figure 5.7: The contributions from the ISGQR and phenomenological background calculated for a similar experiment at iThemba LABS. The phenomenological background is enhanced towards the higher energy part of the spectrum.

Secondly, there is a component of phenomenological background from quasi-free scattering as well as higher energy contributions from multipolarities above $L = 2$. This scattering generally forms the main contribution of background in energy regions above 20 MeV [64]. A method of experimentally estimating this background is by finding a region where there is a negligible contribution from E1 photons and determining a parameterization for this background in the region of interest. This has been done in the case of the neodymium isotopes [48] and in heavier elements like ^{208}Pb [51]. However, it could not be done in this case because the E1 strength extends well beyond the focal plane acceptance and there is still a contribution from the k_1 peak situated at 24 MeV.

5.2.2 Angular Sensitivity Analysis

What follows is a preliminary study to determine whether the angular data of the K600 using only the 0° aperture is sensitive enough to estimate multipolarity of a state. If successful, the relative strengths can be used in conjunction with finite angle measurements for MDA (Multipole Decomposition Analysis) [69] for future experiments at 0°. By looking at the evolution of states with

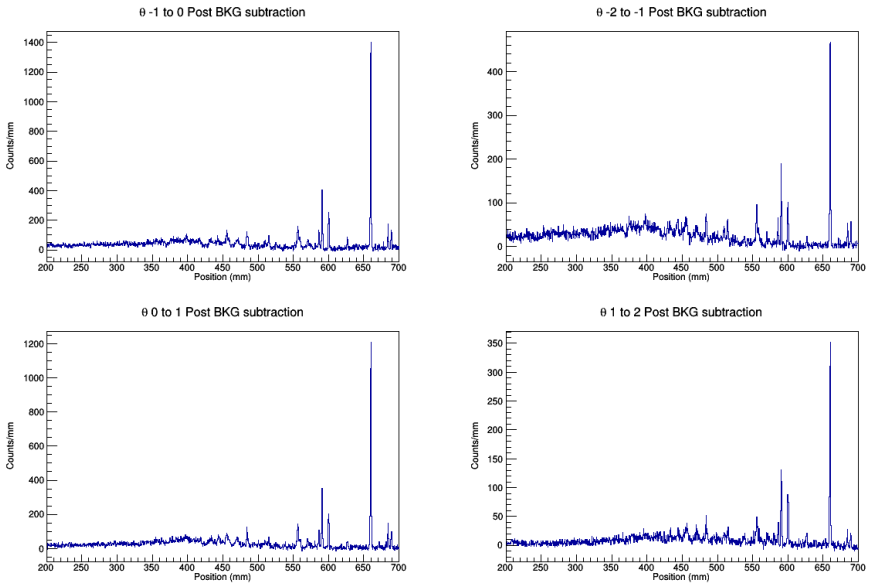

Figure 5.8: The counts spectrum for each region following the background reduction procedure described in Section 4.2.1 . The region between -1 and -2 degrees clearly shows an anomalous behaviour towards the 200 mm side and thus the higher energy region of the detector.

regards to scattering angle the relative strengths of each multipolarity in each angular region can be compared. This can be done using the states that are well resolved in the energy ranges between 9 and 14 MeV. If implemented correctly, the parity of unknown states can also be inferred from their relative strengths.

The scattering angle for the 0° aperture ranges from $-2°$ to 2°. After the background was subtracted in each of these individual regions, the amount of counts in the peaks were then inter-compared. The background reduction process is identical to the process described in Section 4.4.1 except that each spectrum is gated according to the scattering angle. Figure 5.8 shows each angular region after their separate background subtractions. The counts in each prominent peak are plotted in two different ways: First the raw number of counts in each peak is summed over and compared. There should be significant deviation in the number of counts between the 0° to 1° and 1° to 2° regions as the beam is centered around zero degrees. This is seen in the top panel of Fig. 5.9 where the raw number of counts in each state shows a considerable decrease. A relative decrease in the excitation of the spin-flip states are also observed (+0), whereas a relative increase in strength is shown for some of the $+1| + 2$ transitions. Secondly, the trend of each state is drawn relative to its strength at 0° in the bottom panel of Fig. 5.9 and in it this trend is becomes more visible. This is

in agreement with some of the findings using heavier isotopes such as seen in angular spectrum analysis done on ^{120}Sn using the Grand Raiden Spectrometer at RCNP [70]. A drop in strength of 67.7% is observed in the ^{24}Mg spin-flip state at 10.71 MeV from 0° to 2°. It is unclear what percentage of this reduction is purely from the reduced counts in the higher scattering angle acceptance and what percentage is caused by the multipolarity scattering angle dependence. One of the reasons that the excess in counts between 0° and 1° is observed is due to the lack of vertical resolution when the the K600 is set up for zero degree measurements. This poor resolution can lead to many events being shifted to lower scattering angles as shown in Fig. 5.10. This leads an amount of mixing between 0° and 1° and 1° and 2° scattering angle events in the 0° and 1° region that is hard to disentangle. At finite angles the vertical resolution of the K600 is higher and this problem is mitigated. There is a slight dependence on scattering angle that can be obtained using these angular spectrum gates. However, for a more conclusive exploration of this method a comparison to another light isotope with strong spin-flip transitions is required.

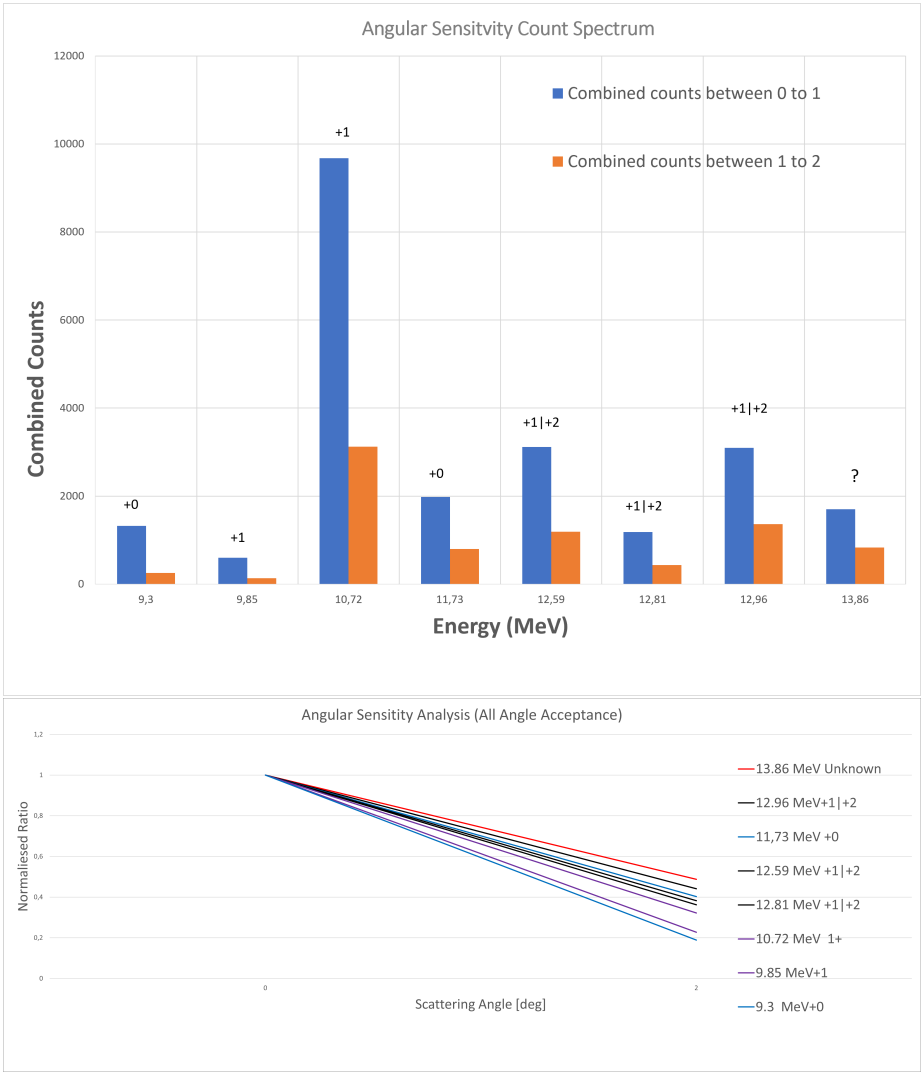

Figure 5.9: Top: Graph showing the amount of counts in each peak and the parity assignments for each of the prominent states in the spectrum for each angle angular gate. Bottom: Graph showing the angular progression of the states normalised to their strength at 0°.

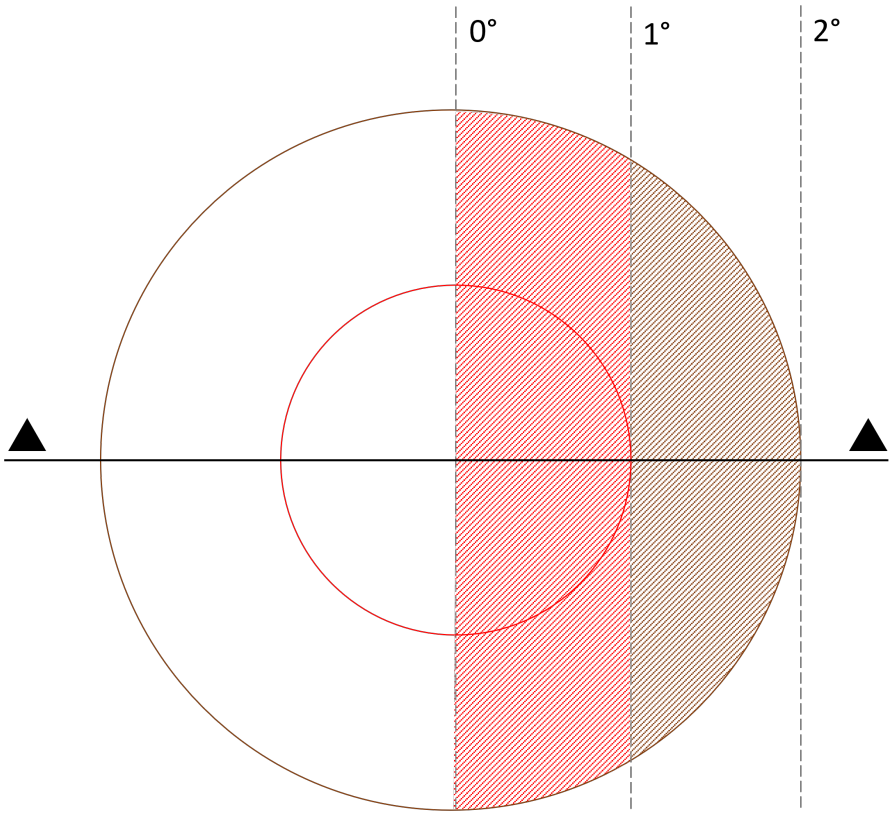

Figure 5.10: A schematic of the aperture showing the solid angle of the detector. The red region corresponds events that can be mapped to a scattering angle between 0° and 1° due to poor vertical resolution and the gray to 1° and 2°.

Chapter 6

Conclusion and Outlook

High energy inelastic proton scattering at 0° was performed on ^{24}Mg at the iThemba LABS facility using the high K600 spectrometer in high dispersion mode. The data gathered was used to investigate the virtual photoabsorption technique in light, deformed nuclei such as ^{24}Mg for use in future experiments proposed by the PANDORA project. The total photoabsorption cross section was successfully extracted using the virtual photon absorption technique applied to (p,p') data for ^{24}Mg in the region of the first peak of the IVGDR. It compared favourably to both a previous experiment on ^{24}Mg done using (γ,abs) and the systematic Lorenzian calculation done using the RIPL database.
The total photoabsorption cross section was successfully extracted using the virtual photon absorption technique applied to (p,p') data for ^{24}Mg in the region of the first peak of the IVGDR. This is an encouraging result for the prospects of the technique especially in the context of nuclear astrophysics. Using this technique, the total absorption cross section for many stable light nuclei up to ^{56}Fe can be extracted for use in UHECR propagation codes. This comes with the added benefit of high resolution spectra for other important quantities such as level densities and neutron thresholds. The angular sensitivity analysis requires more data at larger angles and also data from similar mass nuclei to help verify whether it can be used effectively for future experiments. A DWBA analysis using two-fold macroscopic form factors is also required for this method to be effective. This is in the process of being calculated but was deemed outside the scope of this thesis.
There are methods that can be used in conjunction with the virtual photon absorption to understand the decay behaviour of the IVGDR such as coincidence and branching rate measurements. The CAKE (Coincidence Array for K600 Experiments) system at iThemba LABS can be used for this goal. Finite angle measurements would also grant access to MDA for more accurate multipolarity subtraction. MDA in combination with charged particles coincidence measurements is be part of all the proposed experiments of the PANDORA project. The resulting photoabsorption cross section spectra can then be cross referenced and compared against data from ELI-NP (γ, abs). This has formed

the basis of new experiments given the relative importance of lighter elements such as ^{24}Mg as keystone nuclei in UHECR propagation and nuclear structure. The first set of proposed elements for the PANDORA project are ^{12}C and ^{27}Al at iThemba LABS at 0° and 4° scattering angles. This has been approved alongside 295 MeV (p,p') experiments on ^{12}C, $^{10-11}$B,$^{24-26}$Mg and ^{27}Al at 0° and 4° scattering angles using the Grand-Raiden spectrometer at RCNP-Japan. Overall, the aim of this dissertation has been successfully realised and the method investigated has been shown to be a suitable method for future investigations. However, deformed light nuclei such as ^{24}Mg require finite angle measurements in addition to 0° measurements, along with the addition of coincidence measurements to properly characterise their IVGDR as it extends past the zero degree focal plane energy range of iThemba LABS.

Bibliography

[1]M. Nagano and A. A. Watson, "Observations and implications of the ultrahigh-energy cosmic rays", Reviews of Modern Physics **72**, 689 (2000).

[2]B. M. Schwarzschild, "The highest-energy cosmic rays may be iron nuclei", Physics Today **63**, 15 (2010).

[3]L. J. Watson, D. J. Mortlock, and A. H. Jaffe, "A bayesian analysis of the 27 highest energy cosmic rays detected by the pierre auger observatory", Monthly Notices of the Royal Astronomical Society **418**, 206–213 (2011).

[4]R. Abbasi, M. Abe, T. Abu-Zayyad, M. Allen, R. Azuma, E. Barcikowski, J. Belz, D. Bergman, S. Blake, R. Cady, et al., "Pierre auger observatory and telescope array: joint contributions to the 34th international cosmic ray conference (icrc 2015)", arXiv preprint arXiv:1511.02103 (2015).

[5]T. et al (Particle Data Group), "Review of particle physics", Phys. Rev. D **98**, 030001 (2018).

[6]B. Dawson, M. Fukushima, and P. Sokolsky, "Past, present, and future of uhecr observations", Progress of Theoretical and Experimental Physics **2017**, 12A101 (2017).

[7]K. Greisen, "End to the cosmic-ray spectrum?", Physical Review Letters **16**, 748 (1966).

[8]J. L. Puget, F. W. Stecker, and J. H. Bredekamp, "Photonuclear interactions of ultrahigh energy cosmic rays and their astrophysical consequences.", APJ **205**, 638–654 (1976).

[9]R. A. Batista, D. Boncioli, A. di Matteo, A. van Vliet, and D. Walz, "Effects of uncertainties in simulations of extragalactic uhecr propagation, using crpropa and simprop", Journal of Cosmology and Astroparticle Physics **2015**, 063 (2015).

[10]E. Khan, S. Goriely, D. Allard, E. Parizot, T. Suomijärvi, A. J. Koning, S. Hilaire, and M. C. Duijvestijn, "Photodisintegration of ultra-high-energy cosmic rays revisited", Astroparticle Physics **23**, 191–201 (2005).

[11]D. Boncioli, A. Fedynitch, and W. Winter, "Nuclear physics meets the sources of the ultra-high energy cosmic rays", Scientific reports **7**, 1–10 (2017).

[12]A. Koning, D. Rochman, J.-C. Sublet, N. Dzysiuk, M. Fleming, and S. van der Marck, "Tendl: complete nuclear data library for innovative nuclear science and technology", Nuclear Data Sheets **155**, Special Issue on Nuclear Reaction Data, 1–55 (2019).

[13]R. A. Batista, M. Erdmann, C. Evoli, K.-H. Kampert, D. Kuempel, G. Müller, G. Sigl, A. van Vliet, D. Walz, and T. Winchen, "Crpropa: a public framework to propagate uhecrs in the universe", in Epj web of conferences, Vol. 99 (EDP Sciences, 2015), p. 13004.

[14]R. Aloisio, D. Boncioli, A. Di Matteo, A. F. Grillo, S. Petrera, and F. Salamida, "Simprop v2r4: monte carlo simulation code for uhecr propagation", Journal of Cosmology and Astroparticle Physics **2017**, 009 (2017).

[15]W. Bothe and W. Gentner, "Atomumwandlungen durch γ-strahlen", Zeitschrift für Physik **106**, 236–248 (1937).

[16]M. Goldhaber and E. Teller, "On nuclear dipole vibrations", Physical Review **74**, 1046 (1948).

[17]E. Lipparini and S. Stringari, "Sum rules and giant resonances in nuclei", Physics Reports **175**, 103–261 (1989).

[18]P. F. Bortignon, A. Bracco, and R. A. Broglia, *Giant resonances: nuclear structure at finite temperature* (CRC Press, 2019).

[19]M. Harakeh and A. Dieperink, "Isoscalar dipole resonance: form factor and energy weighted sum rule", Physical Review C **23**, 2329 (1981).

[20]M. N. Harakeh and A. Woude, *Giant resonances: fundamental high-frequency modes of nuclear excitation*, Vol. 24 (Oxford University Press on Demand, 2001).

[21]G. Colò, L. Cao, N. Van Giai, and L. Capelli, "Self-consistent rpa calculations with skyrme-type interactions: the skyrme_rpa program", Computer Physics Communications **184**, 142–161 (2013).

[22]N. L. Nguyen, N. Colonna, and S. De Gironcoli, "Ab initio self-consistent total-energy calculations within the exx/rpa formalism", Physical Review B **90**, 045138 (2014).

[23]S. Krewald, V. Klemt, J. Speth, and A. Faessler, "On the use of skyrme forces in self-consistent rpa calculations", Nuclear Physics A **281**, 166–206 (1977).

[24]T. Inakura, T. Nakatsukasa, and K. Yabana, "Self-consistent calculation of nuclear photoabsorption cross sections: finite amplitude method with skyrme functionals in the three-dimensional real space", Physical Review C **80**, 044301 (2009).

[25]W. Kleinig, V. Nesterenko, J. Kvasil, P.-G. Reinhard, and P. Vesely, "Description of the dipole giant resonance in heavy and superheavy nuclei within skyrme random-phase approximation", Physical Review C **78**, 044313 (2008).

[26]P. Papakonstantinou and R. Roth, "Second random phase approximation and renormalized realistic interactions", Physics Letters B **671**, 356–360 (2009).

[27]D. Gambacurta, "Recent applications of the subtracted srpa approximation", in Epj web of conferences, Vol. 223 (EDP Sciences, 2019), p. 01020.

[28]C. Bertulani, "Key nuclear reaction experiments: discoveries and consequences", Physics today **69**, 58 (2016).

[29]M. G. Redlich, "Similarity between shell model and deformed nucleus wave functions", Physical Review **110**, 468 (1958).

[30]J. M. Eisenberg and W. Greiner, "Nuclear theory", (1987).

[31]H. Steinwedel, J. H. D. Jensen, and P. Jensen, "Nuclear dipole vibrations", Physical Review **79**, 1019 (1950).

[32]H. P. g. Schieck, "The discovery of giant resonances", in *Key nuclear reaction experiments*, 2053-2563 (IOP Publishing, 2015), 17-1 to 17–10.

[33]C. Bertulani and A. Nathan, "Excitation and photon decay of giant resonances from high-energy collisions of heavy ions", Nuclear Physics A **554**, 158–172 (1993).

[34]M. Sharma, W. Borghols, S. Brandenburg, S. Crona, A. Van der Woude, and M. Harakeh, "Giant monopole resonance in sn and sm nuclei and the compressibility of nuclear matter", Physical Review C **38**, 2562 (1988).

[35]I. T. Usman, "Fragmentation of the isoscalar giant quadrupole resonance in low mass 12 ¡ a ¡ 40 nuclei and 2+ level density in 40ca from high energy-resolution (p, p') scattering at 200 mev", PhD thesis (2009).

[36]P. von Neumann-Cosel, "Fine structure of giant resonances: what can be learned", arXiv preprint arXiv:1812.09070 (2018).

[37]H. Matsubara, A. Tamii, H. Nakada, T. Adachi, J. Carter, M. Dozono, H. Fujita, K. Fujita, Y. Fujita, K. Hatanaka, et al., "Nonquenched isoscalar spin-m 1 excitations in s d-shell nuclei", Physical review letters **115**, 102501 (2015).

[38]R. Capote, M. Herman, P. Obložinsk, P. Young, S. Goriely, T. Belgya, A. Ignatyuk, A. J. Koning, S. Hilaire, V. A. Plujko, et al., "Ripl–reference input parameter library for calculation of nuclear reactions and nuclear data evaluations", Nuclear Data Sheets **110**, 3107–3214 (2009).

[39]Y. Gupta, U. Garg, J. Matta, D. Patel, T. Peach, J. Hoffman, K. Yoshida, M. Itoh, M. Fujiwara, K. Hara, H. Hashimoto, K. Nakanishi, M. Yosoi, H. Sakaguchi, S. Terashima, S. Kishi, T. Murakami, M. Uchida, Y. Yasuda, H. Akimune, T. Kawabata, and M. Harakeh, "Splitting of isgmr strength in the light-mass nucleus 24mg due to ground-state deformation", Physics Letters B **748**, 343–346 (2015).

[40]B. Tulupov and M. Urin, "Direct and semidirect neutron radiative capture by medium mass nuclei: a new version of the semimacroscopic description", -2012 **20**, 83 (2012).

[41]Y. Torizuka, K. Itoh, Y. Shin, Y. Kawazoe, H. Matsuzaki, and G. Takeda, "Electroexcitation of giant multipole resonances in ca 40", Physical Review C **11**, 1174 (1975).

[42]P. von Neumann-Cosel and A. Tamii, "Electric and magnetic dipole modes in high-resolution inelastic proton scattering at 0", The European Physical Journal A **55** (2019).

[43]F. L. Wilson, "Fermi's theory of beta decay", American Journal of Physics **36**, 1150–1160 (1968).

[44]M. Thomson, *Modern particle physics* (Cambridge University Press, 2013).

[45]W. Love and M. Franey, "Effective nucleon-nucleon interaction for scattering at intermediate energies", Physical Review C **24**, 1073 (1981).

[46]A. van der Woude, "The excitation and decay of isoscalar giant resonances", in Heavy-ion collisions, edited by G. Madurga and M. Lozano (1982), pp. 351–362.

[47]G. Barton, "Rutherford scattering in two dimensions", American Journal of Physics **51**, 420–422 (1983).

[48]L. Donaldson, C. Bertulani, J. Carter, V. Nesterenko, P. von Neumann-Cosel, R. Neveling, V. Y. Ponomarev, P.-G. Reinhard, I. Usman, P. Adsley, et al., "Deformation dependence of the isovector giant dipole resonance: the neodymium isotopic chain revisited", Physics Letters B **776**, 133–138 (2018).

[49]K. S. Krane, D. Halliday, et al., *Introductory nuclear physics*, Vol. 465 (Wiley New York, 1988).

[50]C. Bertulani, "Theory and applications of coulomb excitation", (2009).

[51]M. Jingo, E. Buthelezi, J. Carter, G. Cooper, R. Fearick, S. Förtsch, C. Kureba, A. Krumbholz, P. Von Neumann-Cosel, R. Neveling, P. Papka, I. Poltoratska, V. Ponomarev, A. Richter, E. Sideras-Haddad, F. Smit, J. Swartz, A. Tamii, and I. Usman, "Studies of the giant dipole resonance in 27al , 40ca , 56fe , 58ni and 208pb with high energy-resolution inelastic proton scattering under 0", The European Physical Journal A **54** (2018).

[52]A. Horadam, "Gegenbauer polynomials revisited", The Fibonacci Quarterly **23**, 294–299 (1985).

[53]A. Krugmann, "Off-yrast low-spin structure of deformed nuclei at mass number a 150", (2014).

[54]R. Neveling, F. Smit, H. Fujita, and R. Newman, *Guide to the k600 magnetic spectrometer*, 2009.

[55]R. Neveling, private communication, Sept. 2020.

[56]S. Ritt, P. Amaudruz, and K. Olchanski, "The midas data acquisition system", in Proc. ieee 10th real time conf. (1997), pp. 309–312.

[57]A. K. Dutta and Y. Hatanaka, "Design and performance of the mesh-type high-speed silicon optical position-sensitive devices", IEEE transactions on electron devices **38**, 498–504 (1991).

[58]R. Neveling, H. Fujita, F. Smit, T. Adachi, G. Berg, E. Buthelezi, J. Carter, J. Conradie, M. Couder, R. Fearick, et al., "A high energy-resolution zero degree facility for (p, p) and (p, t) reactions", in Journal of physics: conference series, Vol. 312, 5 (IOP Publishing, 2011), p. 052016.

[59]H. Fujita, Y. Fujita, G. Berg, A. Bacher, C. Foster, K. Hara, K. Hatanaka, T. Kawabata, T. Noro, H. Sakaguchi, et al., "Realization of matching conditions for high-resolution spectrometers", Nuclear Instruments and Methods in Physics Research Section A: Accelerators, Spectrometers, Detectors and Associated Equipment **484**, 17–26 (2002).

[60]U. Rohrer, "Computer programs for designing, investigating and commissioning charged particle beam lines", Scientific and Technical Report 2000, 24 (2001).

[61]I. Antcheva, M. Ballintijn, B. Bellenot, M. Biskup, R. Brun, N. Buncic, P. Canal, D. Casadei, O. Couet, V. Fine, et al., "Root—a c++ framework for petabyte data storage, statistical analysis and visualization", Computer Physics Communications **182**, 1384–1385 (2011).

[62]W. Ewbank, *Evaluated nuclear structure data file (ensdf) for basic and applied research*, tech. rep. (Oak Ridge National Lab., 1977).

[63]P. Kunz, E. Rost, and R. Johnson, "Particle transfer reactions on deformed nuclei", Physical Review **177**, 1737 (1969).

[64]S. Bassauer, P. von Neumann-Cosel, P.-G. Reinhard, A. Tamii, S. Adachi, C. Bertulani, P. Chan, A. D'Alessio, H. Fujioka, H. Fujita, et al., "Electric and magnetic dipole strength in sn 112, 114, 116, 118, 120, 124", Physical Review C **102**, 034327 (2020).

[65]Y. Sakemi, H. Sakaguchi, M. Yosoi, H. Akimune, T. Takahashi, A. Yamagoshi, A. Tamii, M. Fujiwara, K. Hatanaka, K. Hosono, et al., "Zero-degree proton inelastic scattering to the 1+, t= 0 and t= 1 states in c 12", Physical Review C **51**, 3162 (1995).

[66]L. Donaldson, private communication, Sept. 2021.

[67]B. S. Dolbilkin, V. A. Zapevalov, V. A. Korin, L. E. Lazareva, and F. A. Nikolaev, "Gamma-ray absorption cross sections of *sup*19f, *sup*24mg, and *sup*40ca in the 10- to 30-mev energy region.", Izv. Akad. Nauk SSSR, Ser. Fiz., 30: 349-58(Feb. 1966).

[68]I. Poltoratska, R. Fearick, A. Krumbholz, E. Litvinova, H. Matsubara, P. von Neumann-Cosel, V. Y. Ponomarev, A. Richter, and A. Tamii, "Fine structure of the isovector giant dipole resonance in pb 208: characteristic scales and level densities", Physical Review C **89**, 054322 (2014).

[69]T. Wakasa, H. Sakai, H. Okamura, H. Otsu, S. Fujita, S. Ishida, N. Sakamoto, T. Uesaka, Y. Satou, M. Greenfield, et al., "Gamow-teller strength of 90 nb in the continuum studied via multipole decomposition analysis of the 90 zr (p, n) reaction at 295 mev", Physical Review C **55**, 2909 (1997).

[70]A. Krumbholz, P. von Neumann-Cosel, T. Hashimoto, A. Tamii, T. Adachi, C. Bertulani, H. Fujita, Y. Fujita, E. Ganioglu, K. Hatanaka, et al., "Low-energy electric dipole response in 120sn", Physics Letters B **744**, 7–12 (2015).